Eindhoven University of Technology
University Centre in Svalbard

Hyperspectral Data Cube Compression Techniques and Quality Assessments

A.E. Oudijk
0915545

Supervisors:
Fred Sigernes
Hjalmar Mulders

Master Internship Report

Longyearbyen, June 2020

Acknowledgement

I would like to thank my supervisor Fred Sigernes of the Optics and Atmospheric Research group at UNIS. Fred was always patient with my questions and I learned a lot from his extensive knowledge about hyperspectral imaging. Furthermore, he also taught a course at UNIS, where we made a nice excursion to the Kjell Henriksen Observatory. Fred's office door, and later 'email-door', was always open whenever I had a question about my research or writing.

I would also like to thank my supervisor Hjalmar Mulders especially. Hjalmar is working at the Elementary Processes in Gas Discharges research group at TU/e. I am very grateful that I had the opportunity to do my internship in Svalbard and without Hjalmar, this would not have been possible. During the project Hjalmar supervised me with his unprecedented enthusiasm and creativity.

Furthermore, I would like to thank Lotte van Hazendonk, who performed calibration experiments on the hyperspectral imager in earlier research. Lotte took the time to explain her work to me in person, which was very helpful to me.

Finally, I would like to thank Sivert Bakken, who is a PhD candidate at the NTNU. Sivert provided me with quick, informative and motivational replies on my questions.

Abstract

In the HYPSO (HYPer-spectral Smallsat for ocean Observation) project of the NTNU (Norwegian Univerisy of Science and Technology), a target area is imaged by a low-cost Hyper Spectral Imager (HSI) on board of a small satellite. The project goal is to detect and predict oceanographic phenomena, in order to more quickly act upon them. The HSI continuously stores data about the wavelength and intensity of the target area. The HSI provides spatial and spectral information about oceanographic phenomena, such as algal diversity across the globe. Depending on the infrastructure of the experiment a limited bandwidth of communication links is available, requiring that the amount of data that is sent over, is reduced. Therefore, compression algorithms are a necessity to compress data, without losing the information. In this report reference uncompressed data sets obtained with the HSI are compressed with the H.263, H.264 and H.265 compression algorithms, with various quantization parameter (QP) settings. Several experiments are performed to compare the compressed data sets with the reference, uncompressed data set. The H.265 compression with a QP of 30 adequately reproduces reference data, and is therefore recommended to use for the HSI in the HYPSO project.

Table of Contents

1 Introduction

To perform color imagery from a satellite, NASA launched the LandSat-1 in 1972. The LandSat-1 contained a Multi- Spectral Scanner, consisting of one green and red, and two near-IR spectral bands. With this color imaging technique it was possible to extract information about terrain that is difficult to explore on earth, which is scanned from space [1]. Over the years, color imaging techniques improved significantly, resulting in the development of hyperspectral imaging. In hyperspectral imaging the purpose is to obtain a complete light spectrum for each pixel. This imaging technique leads to interesting possibilities in unraveling surfaces from space, but also from the deep ocean [2].

A push broom Hyper Spectral Imager (HSI) obtains, while it is scanning a target area, a data cube of spectral and spatial information. One advantage of this imaging technique is that it stores data about the wavelength and intensity of the scanned area continuously. From the data cube an image can be constructed with a chosen bandpass. Hyper spectral imaging is interesting to use for a wide amount of applications, for example imaging vegetation to obtain more insight of the structure and physiology of the scanned vegetation [3]. Another example is that it can provide information about oceanographic phenomena, such as algal diversity across the globe. This is of great importance in order to understand more about the effects of climate change [4]. An overview of the importance ocean-colour technology and its applications can be found in report 7 of the International Ocean Color Coordinating Group (IOCCG) [5].

The HYPSO (HYPer-spectral Smallsat for ocean Observation) project of the NTNU (Norwegian University of Science and Technology) SmallSat Lab started in 2018 to develop a small satellite with an HSI onboard [6]. For this purpose, the HSI V6 was developed by Fred Sigernes at UNIS (University Centre), Svalbard [7]. The HSI V6 is calibrated and further optimized to capture the spectrum between wavelengths of 400 and 900 nm in the projects of van Hazendonk [8] and earlier by Henriksen [9]. The HSI V6 produces large data sets. A typical measurement of 3 minutes of one target area creates an uncompressed data file of 10 GB. A typical compression algorithm can reduce the file size by a factor of 10^3. Therefore, compression algorithms are a necessity to compress data, without losing the information. In this way, it is possible to gather more information in the limited storage space available. With lossy data compression, data is lost or at least manipulated, and it is unclear to what extent information is lost as well. In this Master internship report the effects of compression on experimental data sets is investigated in order to prevent losing valuable experimental information.

In the Master internship project of van Hazendonk [8], compressed data was collected. When results were compared a wavelength shift of several nm was observed. Whereas it is impossible to determine if the wavelength shifts were caused by compression in the earlier research. In this report it is discussed that compression may not be the only contribution to the observed wavelength shift, but it certainly has a contribution.

The uncompressed data files are compressed with the xvid, x264 and x265 compression algorithms with different settings. The performance of the x264 (also referred to as H.264) compression algorithm has been evaluated by Santos et al [10], firstly in a simulation environment and secondly in a scene of Indian Pines. It was found that the x264 is a suitable video coding standard for the compression of hyperspectral cubes [10]. Furthermore, the x264 encoding was used in the experiments performed by van Hazendonk [8]. It is chosen to test the xvid and x265 to observe the differences in results from these compression algorithms, since the main working principle is very similar, this gave insight on how minor differences in compression could give deviating results. Moreover, it is determined which section of the compressed data is most suitable for wavelength calibration.

The process on how the compression takes place, plays a major role in the application of this HSI due to limited processing resources and a limited bandwidth of communication links. However, this report is limited to giving an overview of determining the quality of the data after compression and not on the compression process details. More information about a compression process can for example be found in Orlandić et al [11], where the possibility for a parallel FPGA (Field-programmable Gate Array) implementation of the CCSDS-123 (Consultative Committee for Space Data Systems) compression algorithm on the small satellite is investigated.

In this report firstly a theoretical introduction is given about the HSI V6. In this theory chapter, the working principle and relevant parameters of the HSI V6 are briefly described along with the working principle of compression algorithms. Secondly, the experimental set-up and strategy is explained along with a motivation for the chosen compression algorithms. The experimental results are discussed, followed by the final conclusion. Lastly, a suggestion is given for future research and applications.

2 Theory

2.1 Working principle Hyper Spectral Imager (HSI) V6

Figure 1: The HSI V6 operates by scanning the landscape. The aperture is line shaped and it allows the recording of the full spectral information for every pixel on each line. By scanning the HSI across the landscape, the HS-image of the landscape can be recorded. An illustration of the pushbroom technique of the HSI V6 can be seen here. The HSI V6 is mounted on a rotating platform. The HSI V6 first gathers one line of spectral information in one spatial dimension, and then as the platform starts rotating slowly, the next line of spectral information is gathered.

In this report, the HSI V6 makes use of the spectral imaging push broom technique. For taking images with this technique of a static area, the imager is put on a rotating platform. The optical system is gathering one line of spectral information in one spatial dimension, as can be seen in the illustration shown in figure 1. The platform starts rotating slowly, and the next line of spectral information can be gathered. While the optical system is moving, information of the second spatial dimension is gathered. These images are all put together to create a full spatial image, in which the third dimension contains the spectral information, see figure 2.

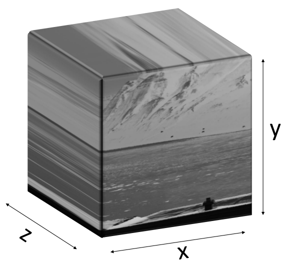

Figure 2: In this illustration an example of a hyperspectral data cube can be seen. The spectral information is stored along the z-axis. The y-axis shows the slit height. The image that can be obtained from the spatial information can be seen on the x-axis. The x-axis is also the direction along which the platform is moving.

2.2 Optical system of HSI

Understanding of basic optical physics is required to understand what pathway the light rays follow. A short overview is given here along with a general explanation of the optical system of an HSI.

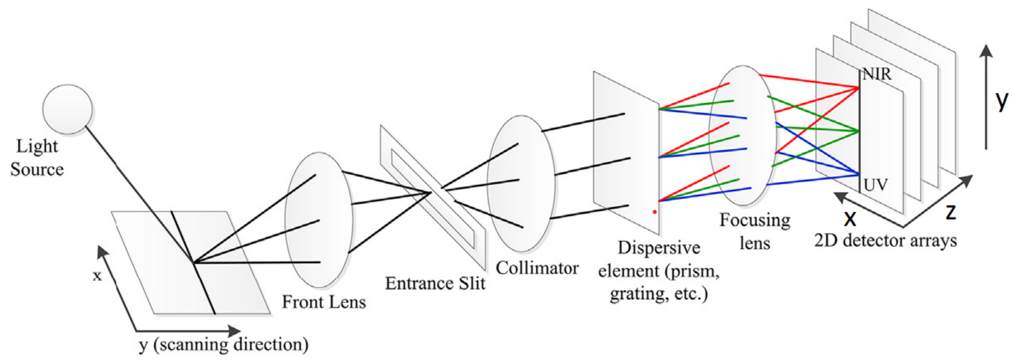

Figure 3: An example of the optical system of a hyper spectral imager from [12]. The entrance slit is positioned at the focal length of the front lens (f_0) and the collimator (f_1). The focusing (detector) lens is distanced from the dispersive element and the detector array with its focal length (f_2). The dispersive element in the HSI V6 is a transmission grating.

The dispersive element in the HSI V6, that can be seen in figure 3, disperses the different wavelengths of the light. The HSI V6 makes use of a blazed transmission grating which is optimized to measure wavelengths in the spectrum of 400-800 nm [7]. The dispersed wavelengths are focused on the detector array. The detector array consists of pixels, numbered 0 to 1919. Building on the calibration results, earlier shown by van Hazendonk [8], the pixel-based line is converted into a wavelength line. It is possible to calibrate each newly detected frame from a picture taken outside with the Fraunhofer lines [13].

Due to the wave properties of light, constructive and destructive interference can occur when two wave sources with different initial phase difference or path difference act together. The main equation describing this is called the grating equation

$$n\lambda = a(\sin\alpha + \sin\beta), \tag{1}$$

where n is the spectral order, λ is the wavelength, a is the groove spacing for a 300 grooves/mm grating, $\alpha = 0$ is the incident angle and β is the diffracted angle, see figure 4.

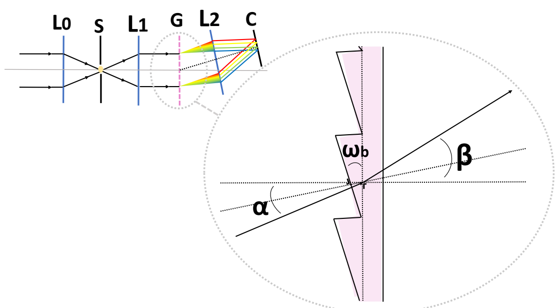

Figure 4: The blazed grating where α is the angle of incidence, β the diffracted angle and ω_b is the blaze angle.

From this equation the angular dispersion is defined as

$$\frac{d\lambda}{d\beta} = \frac{a\cos\beta}{n} \tag{2}$$

If we define $dx = f_2 d\beta$, then linear dispersion becomes

$$\frac{d\lambda}{dx} = \frac{a \cos \beta}{n f_2} \tag{3}$$

2.2.1 Spectral bandpass

The smallest spectral interval that can be isolated or the precision in which a device detects adjacent spectral lines can be described with the bandpass. The bandpass is defined as the Full Width at Half Maximum (FWHM) of a monochromatic spectral line, see figure 5.

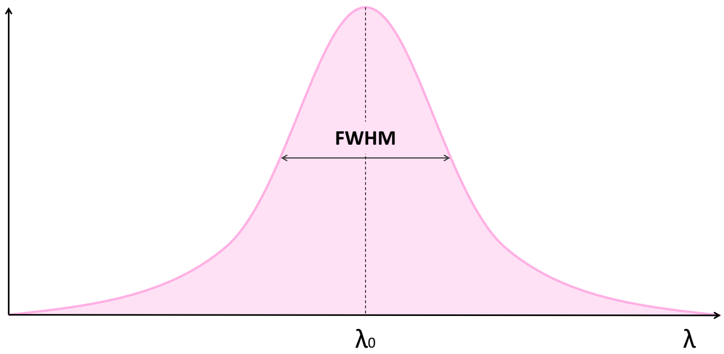

Figure 5: The peak is an illustration of an instrumental line profile of a monochromatic light source with wavelength λ_0. The dotted line shows the source spectrum. The Full Width at Half Maximum (FWHM) is the width of a peak at half the maximum of the amplitude. The FWHM of a spectral line is called the bandpass and can be used to describe the precision in which a hyperspectral imager detects spectral lines.

The recorded spectrum through the spectrometer equals the convolution of the real spectrum of the source that is analyzed and the instrumental line profile. The instrumental line profile equals the convolution of different system properties: Width of slit, natural line width, resolution, alignment, diffraction effects, aberrations or the quality of the optical set-up. The settings of the spectrograph are not used at the limit of resolution and therefore ensure a certain line width, so that the natural line width can be neglected. Furthermore, it is assumed that the instrument is aligned as good that the influence of the slit width is the most important factor on the instrumental line profile and that all the other factors are negligible [14]. So, the instrumental line profile equals the convolution of the width of the entrance slit and the width of the exit slit image[14]. One possible way to calculate the bandpass is by multiplying the linear dispersion, $\frac{d\lambda}{dx}$, by the exit slit image width, w':

$$BP = FWHM \approx \frac{d\lambda}{dx} \times w' \tag{4}$$

2.2.2 Etendue

The area where photons can travel into the optical system define how much light can be detected by the optical instrument. The etendue describes how much space light takes up spatially and angularly.

The etendue (geometric extent), G, is defined as the area of the emitting source (S) times the solid angle (Q) its light propagates into.

$$G = S \times Q \tag{5}$$

The solid angle for the front lens (L_0) in the HSI V6 can be calculated with equation 6, where Ω is the half angle at which the front lens is illuminated by the light source, A is the area that the light source illuminates and p is the object distance. The parameters are also illustrated in figure 6. [14]

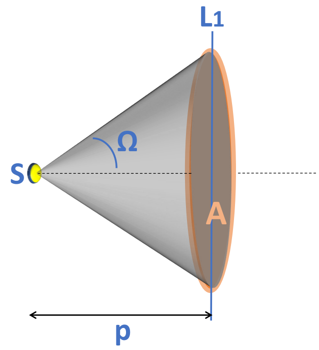

Figure 6: A light source, S, illuminates the front lens L_1 at a distance p under a half angle Ω. The illuminated area is A.

$$Q = \frac{A}{p^2} = \frac{\pi \cdot (p \cdot \sin\Omega)^2}{p^2} = \pi \sin^2\Omega \tag{6}$$

The entrance slit etendue G_2 is given as the area of the entrance slit $(w \cdot h)$ times the solid angle it propagates into, the illuminated grating area $(G_A \cos\alpha)$ divided by the focal length squared f_1^2. Or simply

$$G_2 = \frac{G_A \cos\alpha}{f_1^2} \times w \cdot h. \tag{7}$$

The exit etendue is correspondingly calculated as

$$G_3 = \frac{G_A \cos\beta}{f_2^2} \times w' \cdot h', \tag{8}$$

where w' and h' are the exit slit image width and height images, respectively. The magnification or demagnification of the slit height is given as

$$h' = \frac{f_2}{f_1} \times h. \tag{9}$$

The etendue will never decrease and therefore the components with the smallest etendue dictates the throughput of the system. One important consequence of this property of etendue is that every component in the system's design should complement each other. Throughout the HSI it is desired that the etendue is constant through each of the components, therefore $G_2 = G_3$, from which a relation between the entrance slit width and the exit slit image width results, see equation 10. [14]

$$w' = w \times \frac{\cos\alpha}{\cos\beta} \times \frac{f_2}{f_1} \tag{10}$$

The bandpass of the instrument may now from equation 3, 4 and 10, finally be written as

$$BP \approx \frac{d\lambda}{dx} \times w' = \frac{a\cos\beta}{nf_2} \times w \times \frac{\cos\alpha}{\cos\beta} \times \frac{f_2}{f_1} = \frac{a\cos\alpha}{nf_1} \times w \tag{11}$$

Note in the above equation that the optical bandpass depends mainly on f_1 and the entrance slit width. The theoretical bandpass for the first order diffraction of our instrument becomes 3.3 nm.

2.2.3 Noise

It is possible that a random stray light is detected in the detector array, which can be classified as noise. The ratio of the actual signal and this detected random flux is called the Signal to Noise Ratio (SNR). It is not expected that the signal to noise ratio (SNR) is the same across the entire sensor, due to second-order diffraction that is occurring. Another source of noise in the device is the dark current. Dark current is the phenomenon where, due to electric current that starts flowing in the CMOS sensor without any illumination, counts are still detected. In this report the dark current of the HSI V6 is not investigated. In earlier research by Henriksen [9] and van Hazendonk [8] the dark current is characterized and compensated for in a radiometric calibration. This calibration has been re-used in this report for the creation of images.

2.3 Compression algorithms

2.3.1 Lossless compression

Data that is encoded with lossless compression algorithms conserve the total amount of information. One classic example is the Huffman encoding [15] [16], where the characters are ordered based on the frequency they appear in. A character with a lower frequency is assigned a longer code, whereas a character appearing in a higher frequency is assigned a shorter code. Lossless compressed data has the option to be decoded into the original form if this is considered necessary for processing the data [12]. However, these algorithms can only give limited compression ratios. [10]

Alternatively, one can consider to use a lossy compression. In lossy compression the reconstructed and original image are not identical, allowing for a higher compression. Therefore, the research in this report is focused on a selection of lossy compression algorithms. A broad selection of settings in the algorithms are available so that the user can define which information can be lost or not. Lossy encoding algorithms make use of a combination of different techniques. In the next paragraph a short overview of the fundamental aspects of the first steps of lossy compression algorithms is given.

2.3.2 General Working Principle of Lossy Compression

Typically, the image is divided into macroblocks. Each macroblock consists of three components in color space: The luminance component Y and the chrominance components Cb and Cr. It could be chosen to for example only decrease the color information. After all, the human eye sees luminance more sharply than colors. Therefore, sacrificing colors is a logical decision for picture compression.

Some compression algorithms make use of a Discrete Cosine Transform (DCT) (e.g. the H.261 algorithm) or a similar approach to transform the signal of one image from the spatial domain to the frequency domain. To perform a DCT on a sequence of N-points, first the sequence is mirrored to obtain a $2N$-point sequence. Secondly, the Discrete Fourier Transform (DFT) is taken over this $2N$-point sequence. The DCT is the result of the first N points of the resulting sequence. [16] Now, the high frequency parts of the signal can be removed. The high frequency parts contain detailed information of an image that is hardly visible by the human eye, and can therefore be removed without problems for the apparent quality.

Compression algorithms make use of different Quantization Parameters (QP's), for which in some algorithms a value can be chosen. This parameter controls the amount of compression for every macroblock and scales from 0 to 52. A larger QP value gives a higher compression.

One possibility to compress further is to look at the correlation between neighboring pixels in each frame of an image. Elements that are duplicated, and therefore do not contain new information, are not necessary and called spatial redundancy. Video compression algorithms make use of this phenomenon by using the information of a previous frame to generate a prediction of the current frame. The earlier mentioned macroblocks play a role in this type of compression. The algorithm looks for the macroblock that is most similar to the block that is encoded. For the distance of the macroblock the algorithm starts looking until it has reached a certain threshold. If the distance is lower than the threshold the block is encoded with a prediction benefit; a motion vector is used to describe the encoded macroblock instead of saving the same macroblock as a whole. If a similar macroblock is not found within the specified threshold distance, the macroblock is encoded without a prediction benefit. [16]

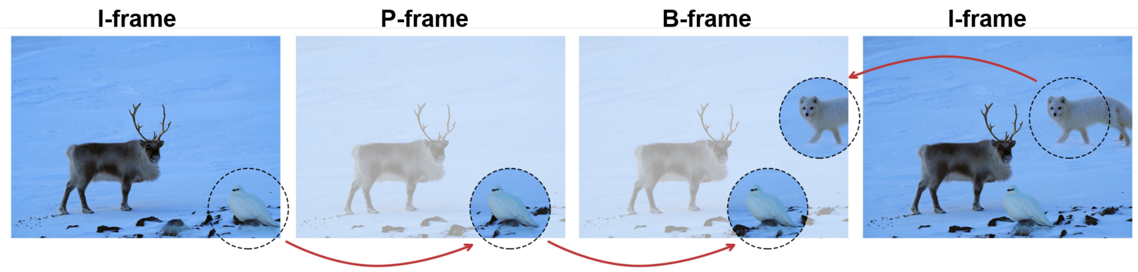

Figure 7: Motion compression principle.

Frames that are coded with motion compensated prediction benefits are referred to as predictive coded frames, called **P**-frames. Some frames are not coded with reference to past or future frames during compression. These frames are specified as, intra coded or **I**-frames. The compression factor of an **I**-frame is lower than the compression factor of **P**-frames because there is no prediction benefit in these frames. The motion prediction of the **P**-frames is based on earlier **I**-frames or **P**-frames. The third frame type is the **B**-frame, the bidirectionally predictive coded frames. A **B**-frame uses motion information from the most recent, past **I** or **P**-frame and motion information from the closest future **I** or **P**. The **B**-frame is never used for the prediction of other frames, and therefore achieves, compared to **I** and **P**, higher compression factors. [16]
An example of the working principle of the **I**, **P** and **B**-frames is given in figure 7. The first **I**-frame on the left side, shows a picture where full detail is maintained. One step to the right, a **P**-frame is observed. To produce this **P**-frame, it is recognized that the picture remains the same as the previous **I**-frame, except for the Svalbardrype that has moved slightly closer to the Svalbard Reindeer. This motion is predicted by the compression algorithm and therefore only the moving vector is saved, resulting in a higher compression. Thirdly, in the **B**-frame, information from both the past and future frame is used to create an image. From the past **P**-frame, similarly as before the moving vector of the Svalbardrype is saved. From the future **I**-frame the movement of the Arctic Fox is recognized, and therefore the arctic fox is already partly showed in this **B**-frame, again using only the moving vector.

3 Experimental Set-up, Protocol and Algorithms

Firstly, the optical system of the HSI V6 is described in this chapter. Secondly the measurement protocol is given. Lastly, the different compression algorithms are shortly described. A complete detailed list of the used equipment can be found in Appendix *A*.

3.1 Optical System HSI V6

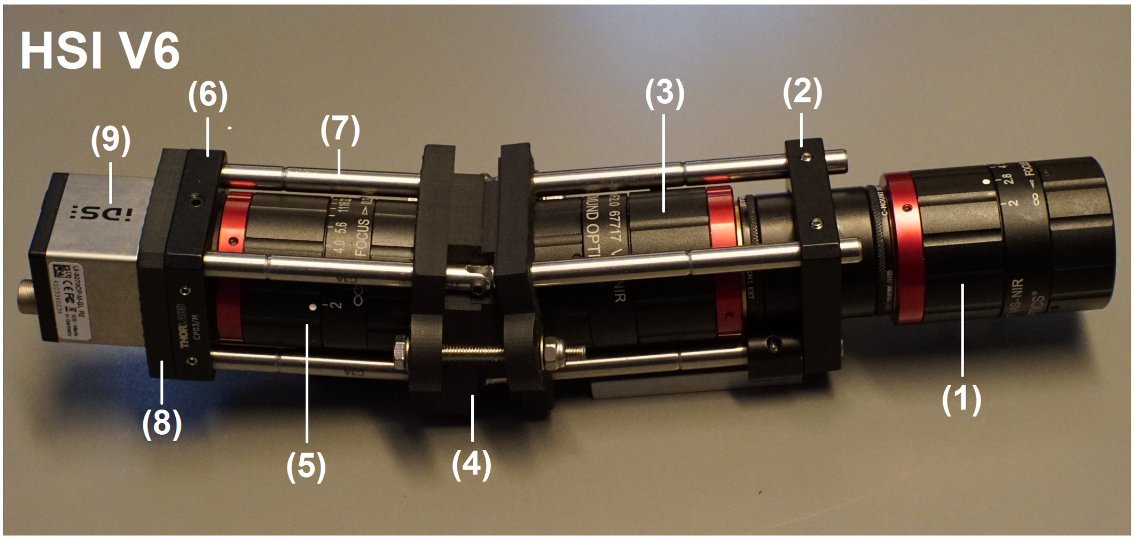

Figure 8: The HSI V6 consists of a front lens (1), CP12 cage plate (2), collimator lens (3), 3D printed grating holder (4), camera lens (5), CP03/M gage plate (6), steel rods (7), a 3D printed camera mount insert (8) and an iDS CMOS camera head (9). This picture is obtained from [7].

In figure 8 the HSI V6 can be seen. The HSI V6 is built by Fred Sigernes at UNIS and has been calibrated and tested before by van Hazendonk [8] and Henriksen [9]. Please note that in the experiments conducted for this report a DMK 33UX174 camera head was used instead of the iDS CMOS camera head shown in figure 8. Furthermore, the HSI V6 is mounted by an aluminium holder on a motion control system to rotate the HSI V6, as can be seen in figure 1.

Light rays that enter the HSI V6, see figure 9, are focused by the front lens (L_0), after which the entrance slit (S) is reached. The entrance slit has a slit height of 7 mm and width of 50 μm. The collimator (L_1) forms a parallel beam that reaches the 300 grooves/mm transmission grating (G). The transmission grating disperses the rays. Lastly, the light rays are focused by (L_2) to the sensor. The lenses (L_0, L_1 and L_2) all have a focal length (f_0, f_1 and f_2) of 50 mm.

3.2 Measurement Protocol

Experiments with the HSI V6 were performed in an optical lab, as can be seen in figure 10. In the optical lab there was a possibility to work in a dark room. The chosen light source illuminates a white board evenly. The HSI V6 (non-rotating) measures the incoming light beams. The data is received uncompressed. Experiments are conducted with a fluorescent tube, these results are used to explore what effects are observed after compression in general. Secondly, a Hydrogen gas discharge lamp was used in the experimental set-up. The intensity peaks of the Hydrogen gas discharge are located at known wavelengths, making them suitable to use as a benchmark. After the experiments, all measurements are compressed with different compression algorithms. With

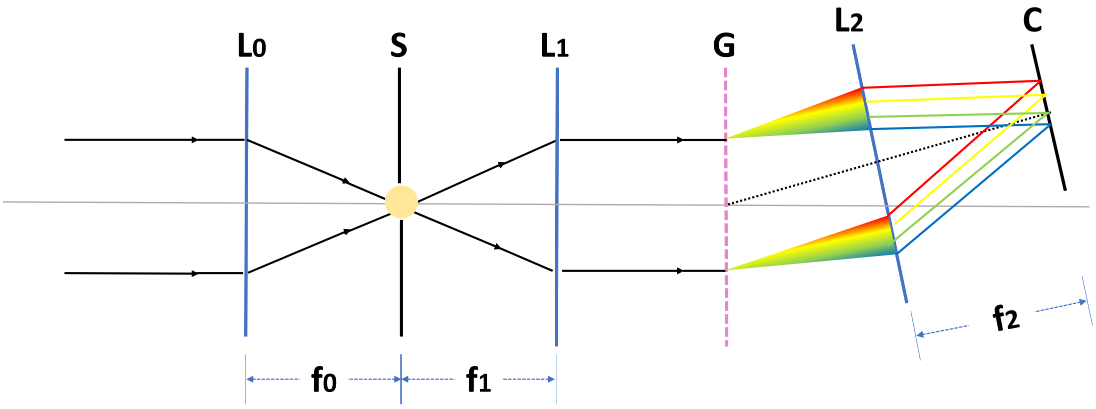

Figure 9: The optical diagram of the spectrograph consisting of a focusing front lens (L_0), an entrance slit (S), a collimator (L_1), a 300 grooves/mm transmission grating (G), a focusing lens (L_2) and a sensor (C).

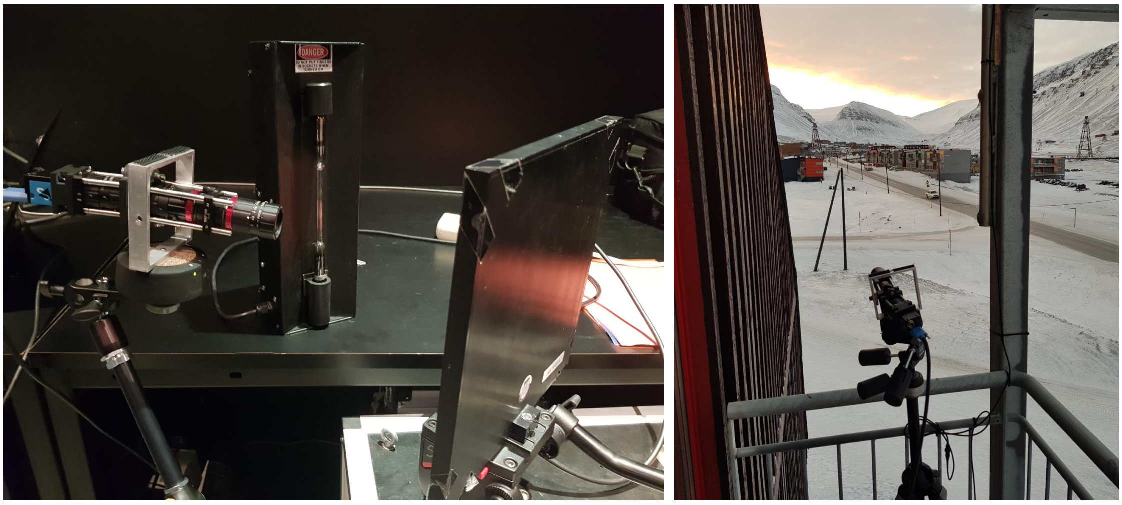

The experimental set-up for performing measurements in the optical lab.

The experimental set-up for performing measurements outside.

Figure 10: Experimental set-up in the lab and outside.

the hydrogen gas discharge the H_α-peak and H_β-peak can be observed in the measurements. The index, spectral bandpass and intensity of these peaks are determined for the uncompressed data set and for the **I**, **P** and **B** frames of the compressed data sets. It is assumed that the unedited, uncompressed data set gives results closest to reality. The average compressed values are compared to the average uncompressed data set.

Finally, measurements were also taken outside, see figure 1 and 10. The Fraunhofer lines are used as calibration points for the wavelength calibration of the images. For each measurement the temperature, humidity, wind speed and air pressure are noted along with the order in which the experiments are performed, to determine if these influence the measurements. The wavelength calibration of a compressed data set and uncompressed data set is compared. Furthermore, from the outside measurements RGB images are created. The images are used to determine the visual quality of the data set. The images created with the uncompressed data set are compared to the images created with the compressed data set. The RGB-pictures are subtracted from each other, after which the intensity scaling is adjusted to show the quality difference between the compressed and uncompressed data sets.

3.3 Methods in Algorithms

Three compression algorithms are researched in this report, the xvid/x263/H.263 compression algorithm, the H.264/x264 compression algorithm and the H.265/x265 compression algorithm.

One lossy algorithm of which several settings are researched is the H.264/AVC encoder [17]. Santos et al [10] showed in their paper that this video coding standard is valid for the compression of hyperspectral cubes. This video encoding standard is widely accepted and commonly used, making it an interesting candidate to investigate the influence on the wavelength calibration in the HSI V6. In this report the H.264/AVC encoder is used with a QP value of 20 and 30. In the remainder of this report this compression method will be referred to as x264.

A second lossy algorithm that is researched is the xvid or H.263 encoding. This algorithm was widely used before the x264 was published and used regularly. The basic working principle is very similar to the x264 encoding [16]. Therefore, this algorithm is chosen to investigate if the improvements that are made for the x264 encoding are not only useful for normal video compression, but also for the encoding of a hyperspectral data cube. One example of an improvement of the x264 algorithm compared to the H.263 algorithm, is that in the H.263 algorithm the smallest macroblock consists of 8×8 components. Whereas in the x264 algorithms the size of macroblocks can be further minimized into sub-macroblocks of size 8×4, 4×8 and 4×4. In the remainder of this report this compression will be referred to as xvid.

Lastly, the H.265 encoder is tested with a QP of 30. The H.265 compression method is the newest method investigated in this report and has not yet been used in experiments with the HSI V6, making it interesting to see if changing the compression algorithm to the H.265 could improve the measurement quality of the HSI V6. In the remainder of this report this compression will be referred to as x265.

4 Results and Discussion

To find out how to compress data without losing too much of the hyperspectral information, several experiments are conducted, achieving uncompressed data files. The uncompressed data files are converged to compressed data sets. A few representative, reference uncompressed test spectra are compared to the compressed data sets. The results are given in this section. Firstly, it is briefly described how the data files are compressed and how different frame types are extracted. Secondly, an overview is given of the compression artefacts that are visually represented in various diagrams, achieved from experiments conducted with a fluorescent tube. In subsection 4.3 experiments with hydrogen are discussed. The index, intensity and bandpass of the H_α-peak are determined for the different compression algorithms to give quantitative insight on the compression effects. From both the Hydrogen and fluorescent tube experiments the x265 with a QP of 30 compressed data file performed most close to the uncompressed data set, with an acceptable compression factor. Therefore, it is chosen to conduct a wavelength calibration on a measurement taken from a Svalbard scenery for the x265 compressed data file to be compared to the uncompressed data file. The wavelength calibration of a QP of 30 and QP of 20 are compared, where it is found that the peak detection is performed with the same accuracy for both QP of 30 and a QP of 20. Finally, an image of the Svalbard scenery is obtained from the x265 QP of 30 compressed and uncompressed data file. The difference between these images two images is minor, resulting from the neat x265 compression.

4.1 Compressing Data Files and Subtracting I-, P- and B-Frames

The experiments for this report are all conducted with achieving uncompressed data files (Y800). The uncompressed data files are compressed with the software of *ffmpeg* [18]. The following lines were used to perform the compression with x264 with a QP of 30 and 20, xvid and x265 with a QP of 30:

```
ffmpeg -i uncompressed.avi -c:v libx264 -qp 30 compressed.mp4

ffmpeg -i uncompressed.avi -c:v libx264 -qp 20 compressed.mp4

fmpeg -i uncompressed.avi -c:v libxvid compressed.mp4

ffmpeg -i uncompressed.avi -c:v libx265 -qp 30 compressed.mp4
```

For each compression a compression factor is determined, which is defined as the size of the reference, uncompressed data file divided over the compressed data file.

Additional information is requested from the compressed data sets in the following way:

```
ffprobe -show_frames -select_streams v:0 compressed.mp4 > C:\IPB_information.txt
```

From the obtained text file, it it determined for each frame from the compressed data set if it corresponds to an **I**-, **P**- or **B**-frame. In chapter 2, it was stated that **I**-frames possibly contain more detailed information than **P**- and **B**-frames, therefore, it is interesting to compare these different frame types.

4.2 Fluorescent Tube

Experiments with a fluorescent tube are conducted to give an overview of the compression effects on an experimental data set. The results are given in this subsection. At first it is visible in table 1 that x264 with a QP of 30 has the highest compression factor, however, later in figure 11, it is shown that this comes with a high distortion. Secondly, figure 12 shows that the x265 compression matches best with the uncompressed data set, with a low standard deviation. Lastly, an example of an **I**, **P** and B-frame is shown in figure 14 from the x265 compression. In this figure it can be observed by eye that the **I**-frame contains more detail than the **P** and **B**-frames. However, the difference between the frames is not significant enough to state that the **I** frames are better to use for peak detection purposes than the **P** and **B**-frames.

4.2.1 Compression Factor

The data set is compressed with different compression algorithms as described in the last subsection. In table 1 the compression factor for each compression algorithm can be seen. Table 1 shows that the x264 algorithm with a QP of 30 has the highest compression factor. The same algorithm with a QP of 20 has the lowest compression factor. In chapter 2 2 it was described that a smaller QP value results in a less compression, therefore it was expected that x264 with a QP of 20 results in a lower compression factor than x264 with QP30. The second highest compression factor, which is nearly as high as the highest compression factor, is received with the x265 compression algorithm with a QP of 30. The xvid compression factor is a factor 10 bigger than the x264 with a QP of 20 compression factor.

Compression Algorithm	**Compression Factor**
x264 QP30	1.87E+04
x264 QP20	6.52E+01
xvid QP 2-31	5.11E+02
x265 QP30	1.43E+04

Table 1: The compression factor for each compression algorithm. The algorithms are used to compress a representative, uncompressed data set achieved with a fluorescent tube. The x264 algorithm with a QP of 30 achieves the highest compression factor. However, the x265 compression factor is nearly as high as the highest compression factor.

4.2.2 Average Compression Effects

The fully obtained data set is a movie consisting of 148 frames. The data is compressed with the xvid, x265 and x264 QP of 30 and a QP of 20. The average centerline of the intensity coming from a fluorescent tube measured over each pixel of the HSI V6, for each compression, can be seen in figure 11. There were no counts detected outside the pixel region of 400 to 1700, therefore not the whole pixel array is shown. With the xvid and the x265 compression, the intensity remains similar to the uncompressed, reference data set, see figure 11. For pixels 750-900 it can be seen that the intensity of both the x264 compressed data files is increased compared to the uncompressed data file. The x264 algorithm lowers the intensity for both QP settings in the region of pixel 400-750 and 950-1100, compared to the uncompressed data file. It can be observed that for a higher refraction, so pixel location 1000 and higher, information is lost in the x264 compressed data files. The peak centered around pixel 850 can be seen in more detail in figure 12.

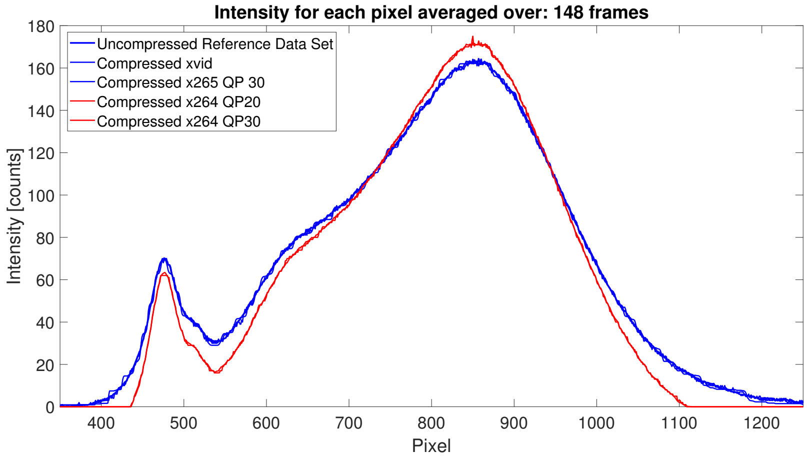

Figure 11: The uncompressed data set, the xvid and x265 compressed data sets are all given in blue, since they are overlapping. For the same reason, the x264 compressed data files are given in red. It can immediately be observed that the x264 compressed data sets show a difference in intensity compared to the uncompressed data file.

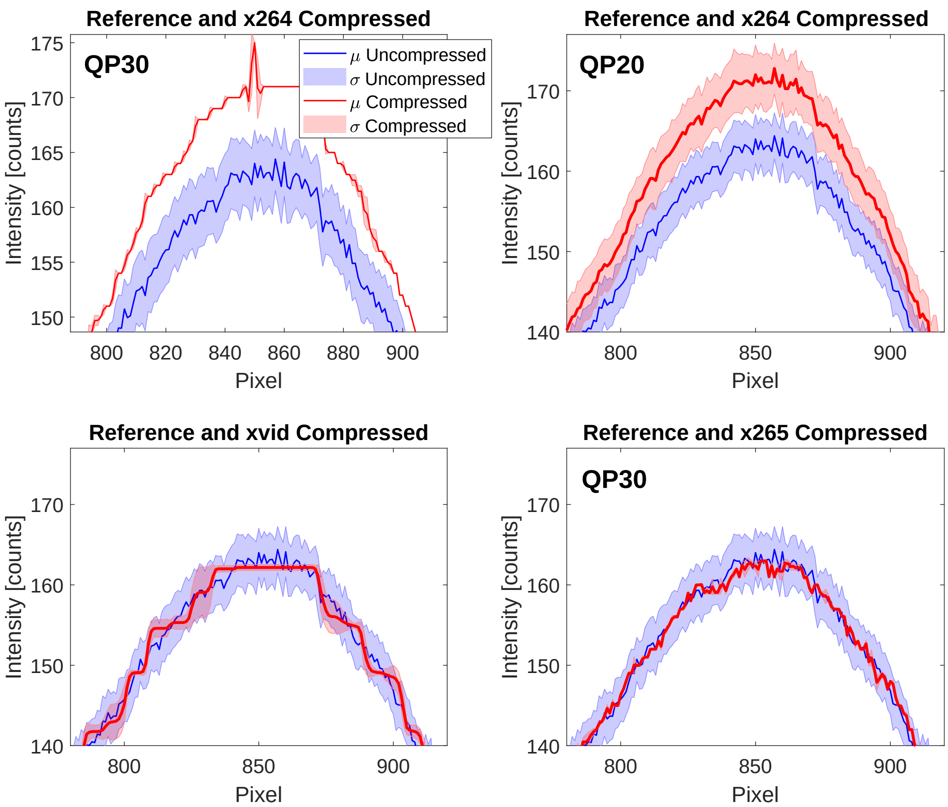

Figure 12: The average intensity coming from a fluorescent tube measured over each pixel of the HSI V6, zoomed in on a pixel range of 780-920. Each figure shows one compressed data set, and the uncompressed reference data set. The standard deviation per pixel, σ, determined from all 148 frames, is shown with a shadow bar around the average graph.

It can be seen from figure 12 that the standard deviation is highest for the compression setting with the lowest compression factor, x264 QP20. It can be observed that the xvid compression shows most difference per pixel range in standard deviation. For example, between pixel 820-830 a higher standard deviation can be observed than for pixel range 840-860. The standard deviation for the compression methods with the highest compression factor, x264 and x264 with QP30 is minor. From the top two figures in figure 12, it can be seen that more detail loss (as can be seen in x264 QP30), results in a lower standard deviation. And that containing detail, results in a higher standard deviation. Depending on the application of the hyperspectral imaging, maintaining the details can be desired. However, one should realize that it is a trade-off between the amount of detail and compression factor.

4.2.3 I, P and B-frames

To perform wavelength calibration, peak detection is necessary. More detail in the measurement results in a more accurate ability in peak detection. In order to assess which frame type is most suitable for wavelength calibration with Fraunhofer lines, the different frame types are also investigated. In the experiments it is observed that the QP of 30 compression loses detail compared to a QP of 20 compression. For all compressed fluorescent tube results it is determined which frame is an **I**, **P** or **B**-frame. The x264 algorithm produced one **I**-frame and 147 **P**-frames for both a QP of 20 and QP of 30. The xvid algorithm produced 13 **I**-frames and **P**-frames. The x265 algorithm produced one **I**-frame, 30 **P**-frames and 117 **B**-frames. The x265 algorithm is therefore the only algorithm that produced all frame types.

In figure 13, only one non-averaged centerline zoomed in on frame 148 can be seen, to show the amount of detail loss for one frame. Frame number 148 is a **P**-frame for all compressed files and represents for the uncompressed data file naturally an **I**-frame. It can be observed that, compared to the reference (uncompressed) data set, all compressed data sets show detail loss. The most detail is lost when using the xvid compression. In x264 with a QP of 30 more flattening can be observed compared to a QP of 20, where the details are very similar to the uncompressed data set. The x265 with a QP of 30 shows similarity in amount of detail to x264 with a QP of 30.

In figure 14 an example of a **I**,**P** and **B**-frame is given from the compressed x265 with a QP of 30. It can be observed that some more detail is conserved in the **I**-frame and most detail is lost in both **B**- and **P**-frames. In order to perform a correct wavelength calibration it could be beneficial to make use of a **I** frame because there is more detail conserved, making it possible to detect the Fraunhofer minimums more accurately. However, the differences are minor for this x265 compression, to investigate if the different frametypes can result in different peak detection a quantitative comparison of the frame types is given in the next subsection.

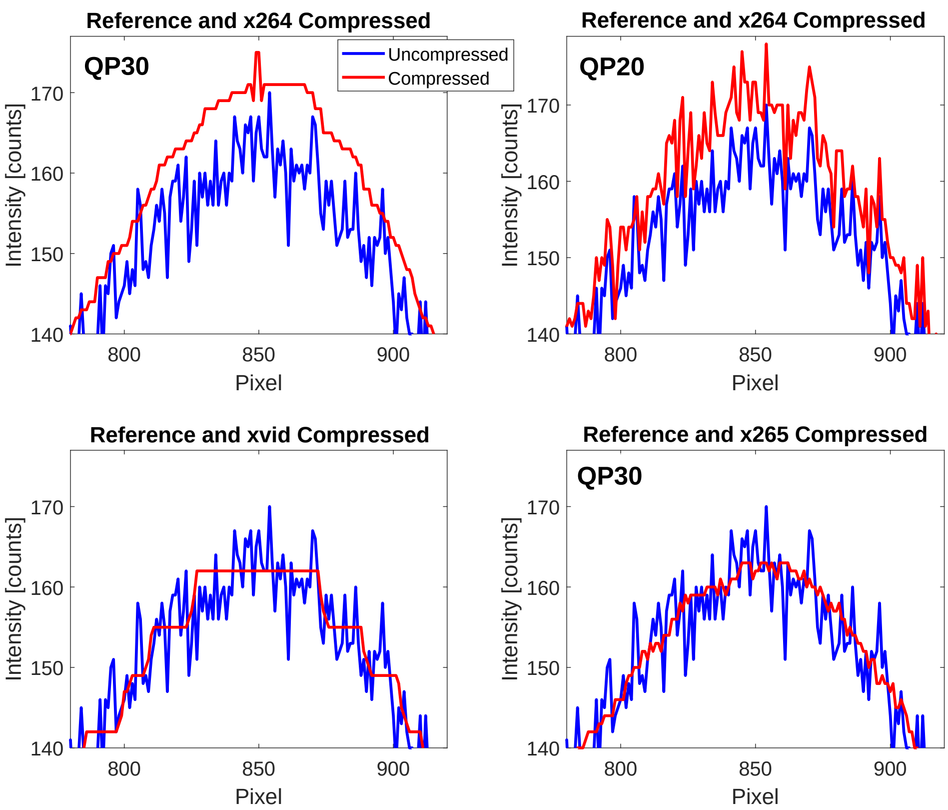

Figure 13: The intensity coming from a fluorescent tube measured over each pixel of the HSI V6. The data is processed with different compression algorithms. It can be observed that most detail is lost when using the xvid compression, but that the intensity remains similar to the uncompressed file. The QP20 and QP30 seem to lower the intensity and detail.

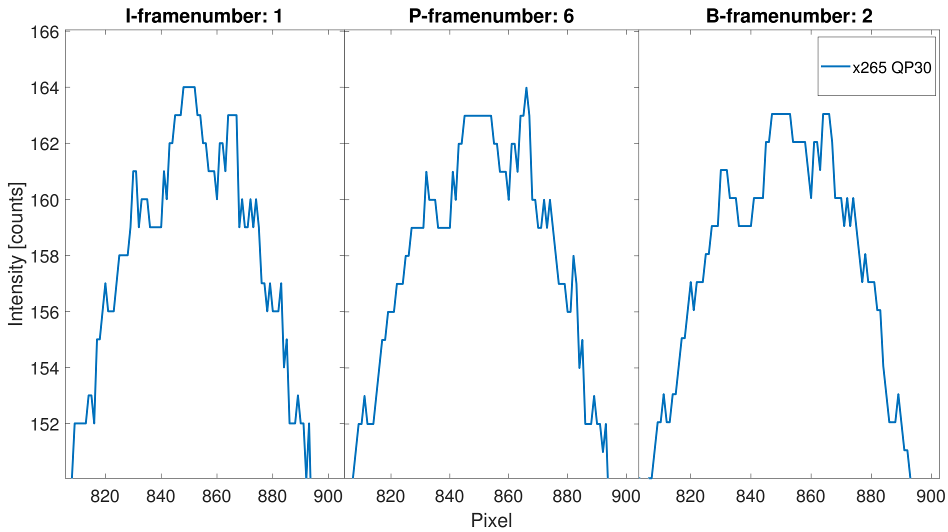

Figure 14: An example of an **I**, **P** and **B**-frame from the x265 with a QP of 30 compressed algorithm. The figure is zoomed to a pixel range of 820 to 900 to show the difference in detail between the different frame types.

4.3 Hydrogen Gas Discharge

In this subsection similar experiments as described before with a Hydrogen Gas Discharge are performed. In the Hydrogen Discharge we see the same behaviour of the various compression methods, the x264 do not reproduce intensity correctly and x265 does. Furthermore, x265 achieves the best compression effects. Just like the experiments conducted with the fluorescent tube, this is a second proof of a good achieved compression with x265 with a QP of 30.

4.3.1 Compression Factor

In this chapter a measurement of hydrogen consisting of 1010 frames is studied. The measurement is recorded with a gain of 5.3dB, exposure time of 1 second and an Auto reference of 128 without any compression (Y800). The compression factors after each compression can be seen in table 2. The x265 algorithm with a QP of 30 achieves the highest compression factor, followed by the x264 with a QP factor of 30 and 20, respectively. The lowest compression factor is achieved by the xvid algorithm.

Compression Algorithm	Compression Factor
x264 QP30	2.30E+04
x264 QP20	1.66E+04
xvid QP 2-31	7.22E+02
x265 QP30	1.46E+05

Table 2: The compression factor for the compression algorithms used to compress the data set achieved with a Hydrogen Gas Discharge. The x265 algorithm with a QP of 30 achieves the highest compression factor.

4.3.2 Average Compression Effects

In figure 15 and figure 16 the averaged intensity centerline along with the standard deviation of the H_α and H_β peak over 402 frames from one experiment can be seen. The experiment is conducted with stable conditions. Therefore, theoretically, every frame should give the same measurement result. In practice the set up with the HSI V6 is not a perfect set up. Therefore, not every frame gives the exact same result, resulting in a standard deviation of the mean. The blue line in figure 15 and figure 16 shows the raw uncompressed data set and is therefore assumed to be the most reliable result. Therefore, the compressed datasets are compared to the uncompressed data set.

The top graphs represent the x264 compression with a QP of 30 and 20, respectively. The intensity of both x264 compression algorithms is lower and shows a smaller bandpass than the intensity of the uncompressed graph in figure 15. In figure 16, the opposite effect can be observed, here the x264 compression algorithms achieve a higher intensity. The xvid compression is visualized in the bottom left graph and shows in figure 15 a similar intensity as the uncompressed algorithm, however it seems that the bandpass is larger for the xvid compression than for the uncompressed data set. In figure 16 the intensity of the xvid compression is lower than the intensity of the uncompressed dataset. The x265 algorithm with a QP of 30, shown in bottom right, shows the most similarity to the uncompressed data set in terms of intensity and bandpass, both in figure 15 and 16.

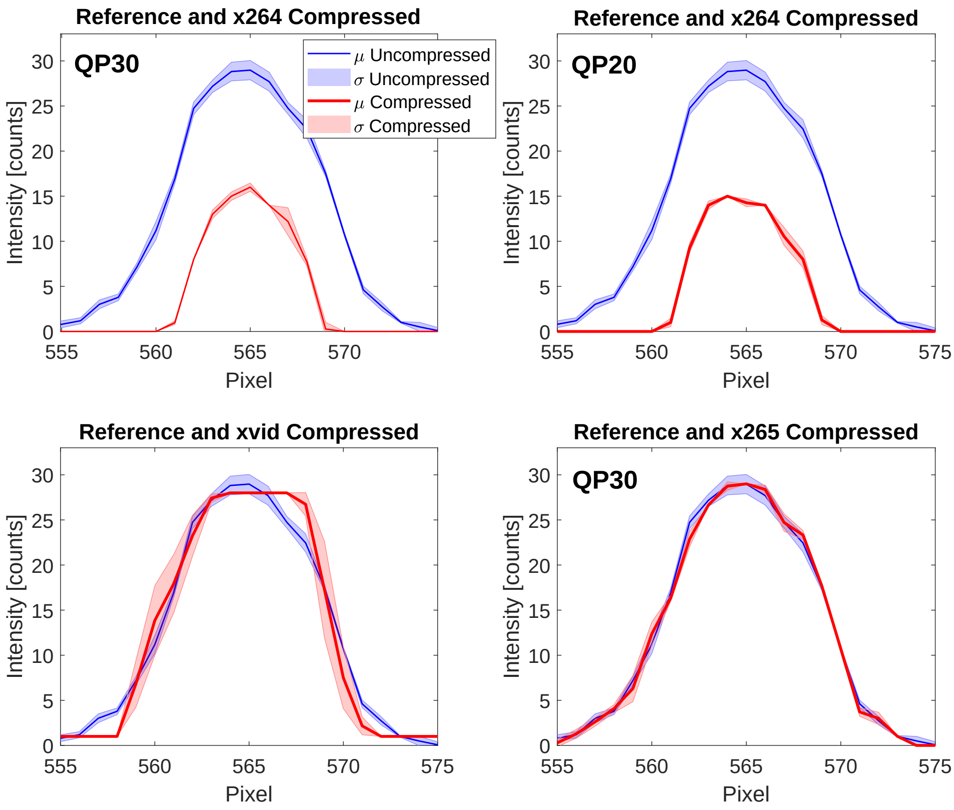

Figure 15: The intensity of the H_β-peak for different compression algorithms.

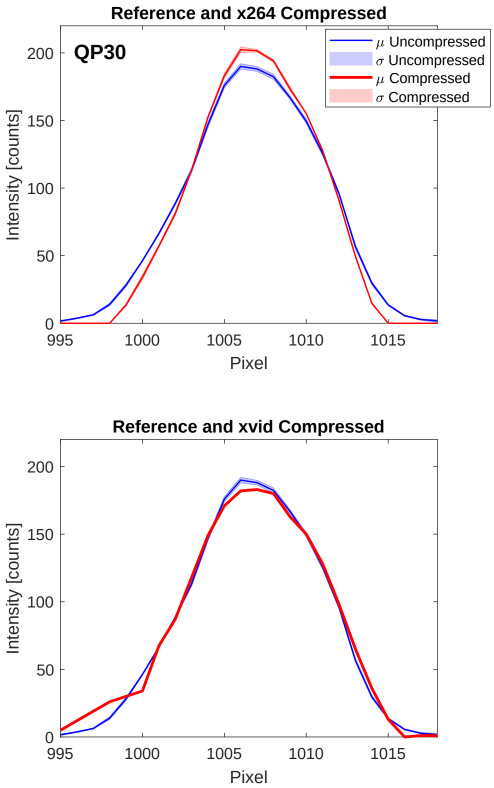

Figure 16: The intensity of the H_α-peak for different compression algorithms.

4.3.3 Quantative Comparison

For all compressed hydrogen gas discharge it is determined which frame is an **I**, **P** or **B**-frame. The x264 algorithm produced 7 **I**-frames, 255 **P**-frames and 748 **B**-frames for both a QP of 20 and QP of 30. The xvid algorithm produced 85 **I**-frames and 925 **P**-frames. The x265 algorithm produced 5 **I**-frames, 198 **P**-frames and 807 **B**-frames. The xvid algorithm is therefore the only algorithm that did not produce all type of frames.

The index, intensity and bandpass of the H_α-peak are determined separately for each frame for the uncompressed data set and each compressed data set. The average results for each frame type are shown in figure 17. In every graph in figure 17 the reference (uncompressed) data set is shown for clarity, but naturally the uncompressed data set consists of **I**-frames only. The standard deviation in the average reference measurement is shown with the dotted blue vertical lines.

In figure 17, the index of the H_α-peak of the x264 compressed data sets is determined within the range of index determination of the uncompressed data set. Furthermore, the x264 compressed data sets show, as already seen in figures 11, 15 and 16 an intensity count deviating from the uncompressed data set. Lastly, the average FWHM of the x264 compressed data set appears sharper than in uncompressed data set, implying to achieve a higher accuracy than the uncompressed data set, which is theoretically not possible.

For the xvid compressed data set it can be seen that the index, intensity and bandpass are incorrectly determined compared to the uncompressed data set. This holds for both the **I** and **P** frame types.

For the x265 compressed data set it can be observed that the index is determined correctly within the range of the uncompressed data set for both **I**-frames and **P**-frames. The **B**-frames show a bigger chance of determining the index of the H_α peak outside of the uncompressed index range. The intensity is determined within the uncompressed data set range for all frame types. The bandpass of the x265 compression is, compared to the other compressed data sets, determined most closely to the uncompressed data set. From the results seen in this subsection, the x265 compression algorithm has a neat compression factor and matches the uncompressed data set results. Therefore, the wavelength calibration of a x265 compressed data set is compared to a wavelength calibration of an uncompressed data set in the next subsection. Furthermore, an image acquisition of a x265 compressed data set and an uncompressed data set of a Svalbard scenery is shown in the next subsection.

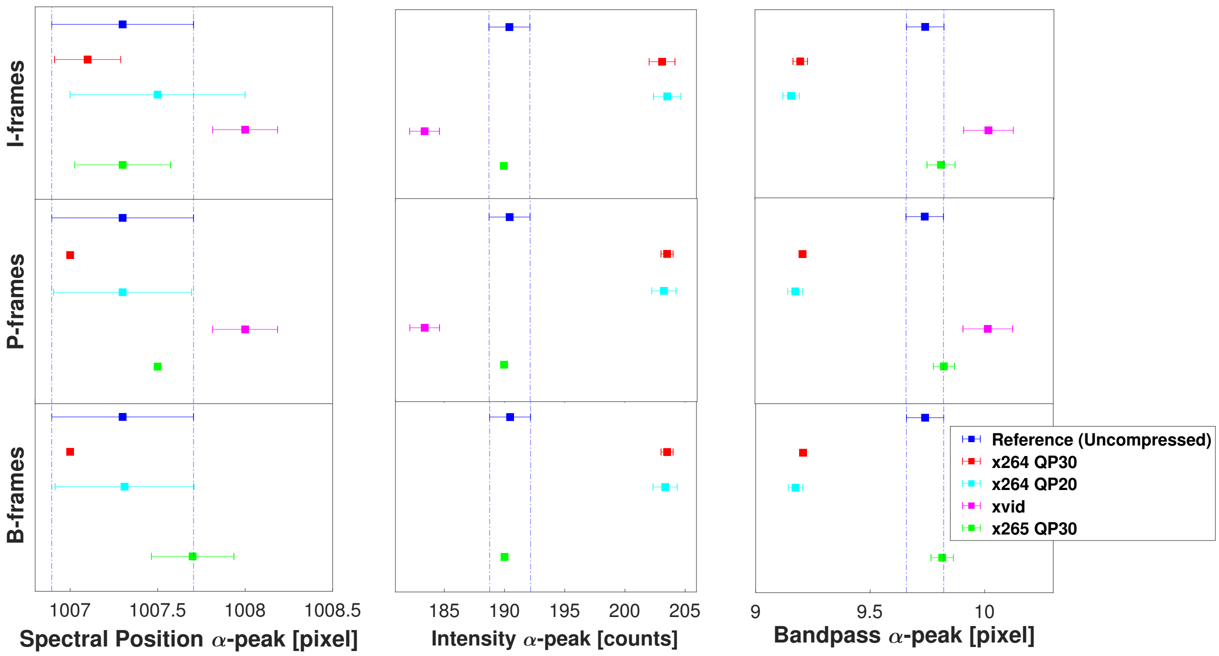

Figure 17: Average spectral position, intensity and bandpass for H_α, with the corresponding standard deviation. The standard deviation of the reference data points is shown within the dotted blue lines.

4.4 Wavelength Calibration Using Fraunhofer Lines

In this chapter an uncompressed measurement from a Svalbard scenery is taken and compressed with x265 and a QP of 30. The x265 compression is chosen because it performed most closely to the uncompressed data set in the earlier described experiments. The compression factor for this measurement is equal to $3.7 \cdot 10^3$. The compressed data set consists of 22 **I**-frames, 1046 **P**-frames and 4267 **B**-frames.

The centerline of frame number 501 (an **I**-frame) can be seen in figure 18. In this figure it can be observed that the compressed data set overlaps neatly with the uncompressed data set, as expected from the earlier results. To produce an image from the measurement, first a wavelength

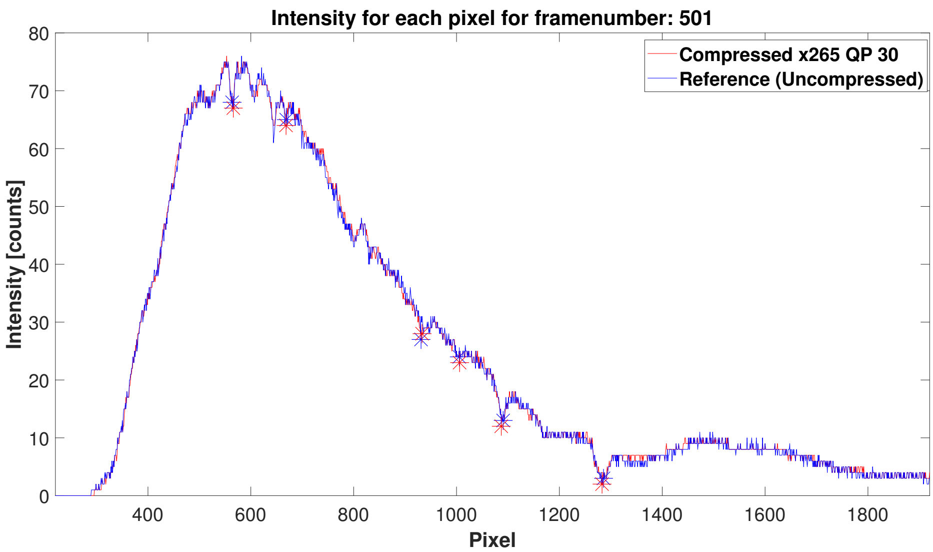

Figure 18: The x265 with a QP of 30 compressed and uncompressed centerline of frame number 501 (**I**-frame), from a measurement of a view of the port of Svalbard, can be seen here. It can be seen that the centerlines nicely overlap.

calibration is performed. The wavelength calibration is performed in a similar fashion as described in in Henriksen [9] and later improved by van Hazendonk [8]. In figure 18, a certain pixel range is determined by eye in which the Fraunhofer lines are recognized. Within this range, the minimum is determined in the exact same manner as the maximums of the H_α-peak maximums are determined. If more than one index is found for a minimum within the specific range, the mean value of these minimums is determined to be the finial minimum value. The found minimums are shown with a star in figure 18 and more clearly in figure 19. In figure 19 it can be seen that the minimums are not determined at the same location for the compressed and uncompressed data set.

With the known Fraunhofer lines and with the minimum pixel indices determined to be located at the Fraunhofer lines, the pixel wavelength correlation can be determined as in 12.

$$\lambda \approx a_0 + a_1 \cdot [idx] + a_2 \cdot [idx]^2 \tag{12}$$

In equation 12, λ represents the wavelength in nm, idx is the measured pixel index and a_0, a_1 and a_2 are constants to be determined from the wavelength calibration.

This wavelength calibration was conducted for the compressed (x265) and uncompressed data set, the result for frame number 501 can be seen in figure 20, where the compressed and uncompressed centerline remain overlapping neatly.

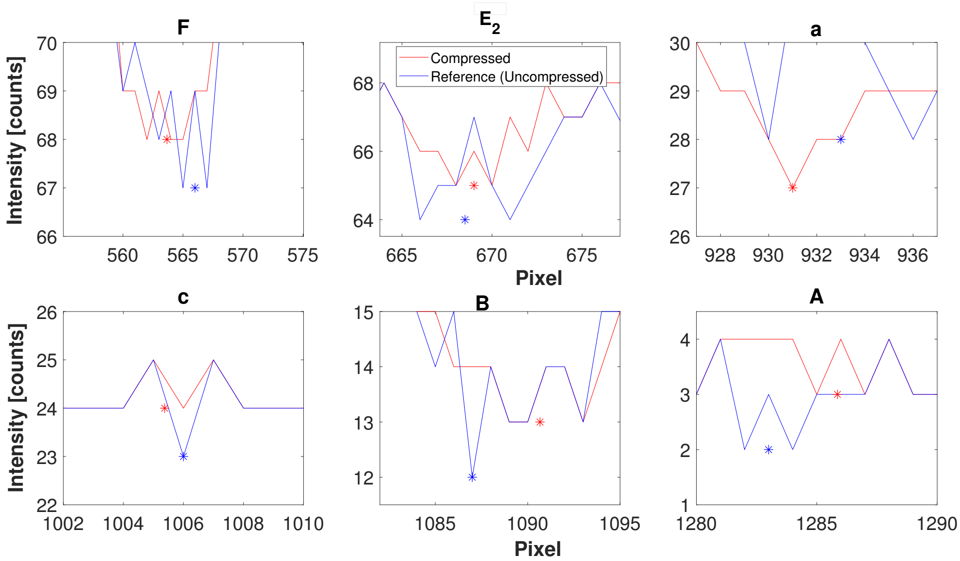

Figure 19: Within a certain pixel range it is recognized that a Fraunhofer line is present, for example the Fraunhofer line F is recognized to be in the pixel range of 555 and 575. This detected minimum (star) can be seen on the top left of the images, followed by the E_2, a, c, B and A location. It can be seen that the detected minimums of the compressed and uncompressed data sets are not equivalent.

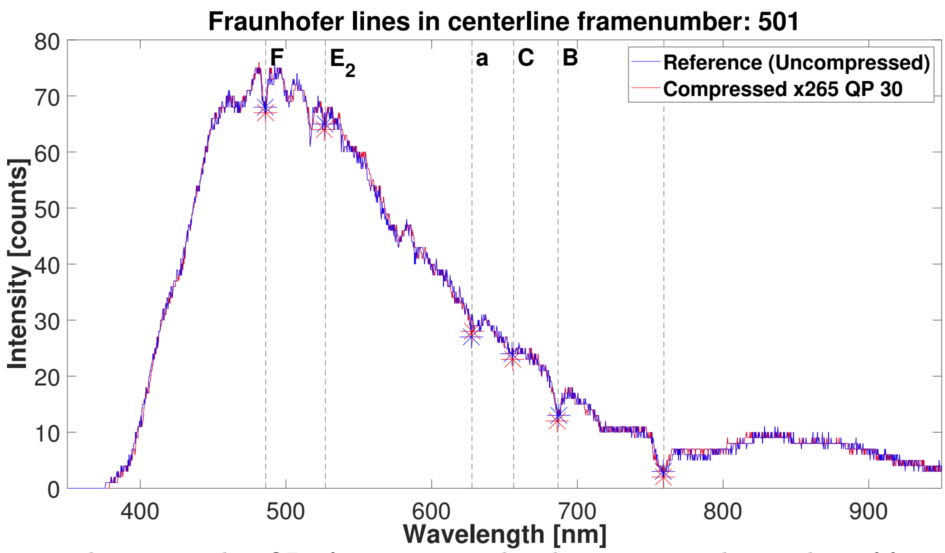

Figure 20: The x265 with a QP of 30 compressed and uncompressed centerline of frame number 501 (**I**-frame), from a measurement of a view of the port of Svalbard, after wavelength calibration can be seen here. It can be seen that the centerlines nicely overlap. The Fraunhofer lines F, E_2, a, c, B and A on which the wavelength calibration took place, are also shown in dotted vertical lines.

The location of the minimums can be observed as a function of wavelength more closely in figure 21, where the minimums are not exactly overlapping, however they remain within 1 nm of each other. To observe whether the choice of frame-type can influence the correctness of minimum determination of the compressed data file, this wavelength calibration was conducted for all frames. For all frames the absolute difference minimum location for the compressed and uncompressed

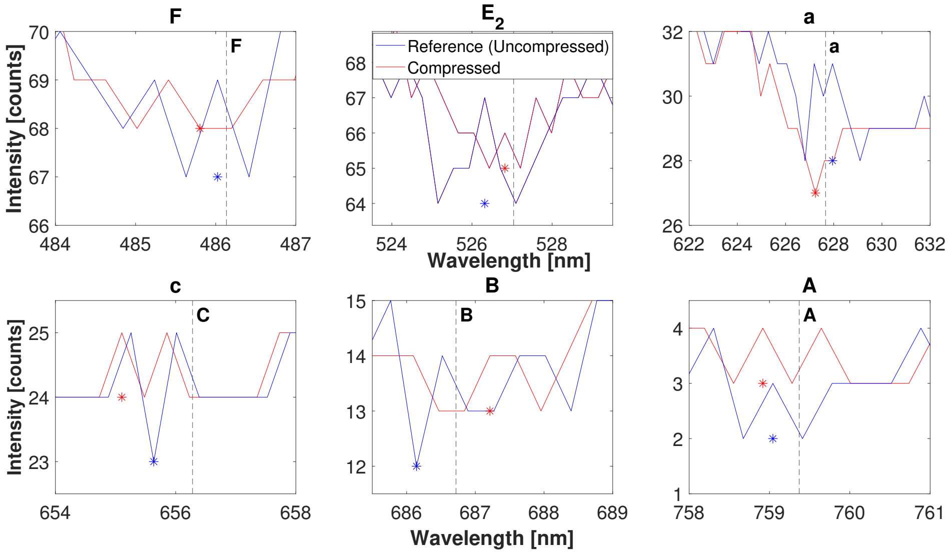

Figure 21: The detected minimums (star), that are used to perform the wavelength calibration are shown here. The Fraunhofer lines used are F, E_2, a, c, B and A and are marked with a vertical dotted line. It can be seen that the detected minimums of the compressed and uncompressed data set are not equivalent.

frame (ΔIndex) is determined. The average difference, along with a 68% standard deviation interval, can be seen in figure 22. Only the **B**-frame type shows a slightly bigger interval with which the index can differ from the compressed and uncompressed data set and could therefore be avoided to use for wavelength calibration. The **P**-frames show the smallest difference in compressed and uncompressed index. However, these results are minor and show no significant difference in peak determination in the different frame types. In earlier experiments with the Fluorescent Tube set up, it was shown that an x264 with a QP of 20 compression results in more remaining detail. To evaluate if the higher amount of detail results in a better peak detection the same wavelength calibration for a x265 compression with a QP of 30 is performed, see Appendix B. In figure 22, also the ΔIndex of the compression with x265 with a QP of 20 is shown. However, there is no significant improvement in peak detection found.

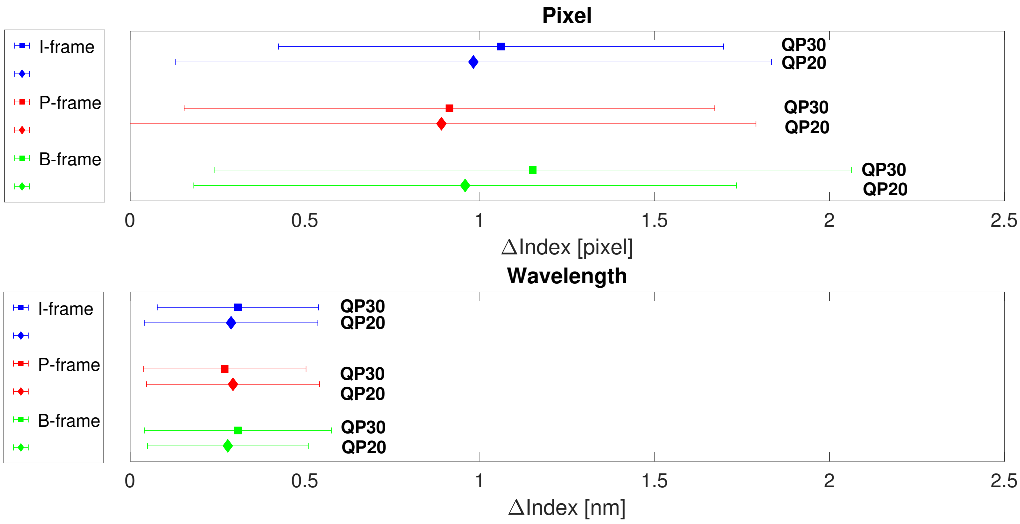

Figure 22: The difference in index and between the compressed and uncompressed data sets has maximum of 2 pixels for all frame types. After the wavelength calibration the difference in index between the compressed and uncompressed data sets has a maximum of 0.6 nm. Little difference between different frame-types can be observed before and after wavelength calibration.

4.5 Image Svalbard Scenery

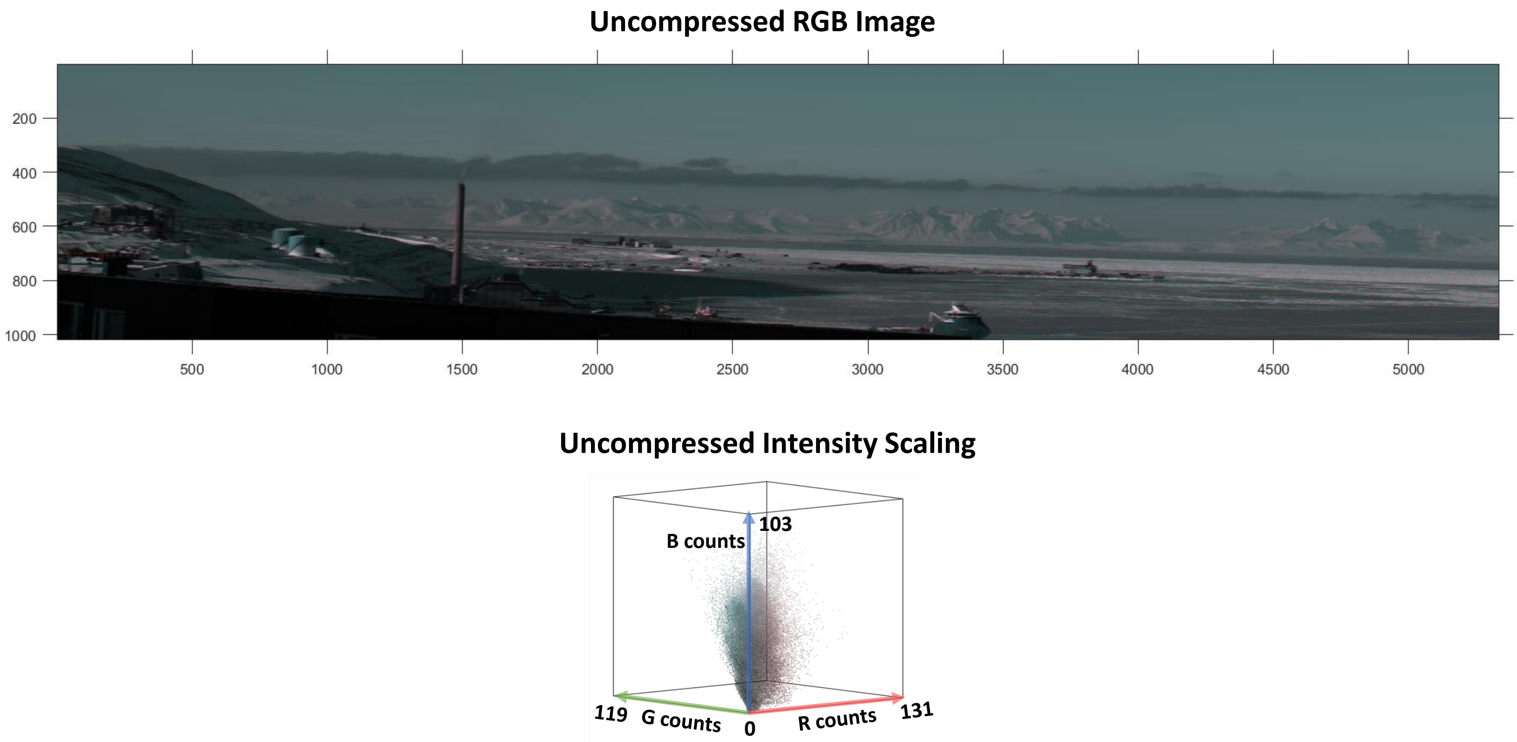

Figure 23: The image obtained from the uncompressed data set. The image shows a view of the port of Svalbard on clear day, along with an intensity scatter plot.

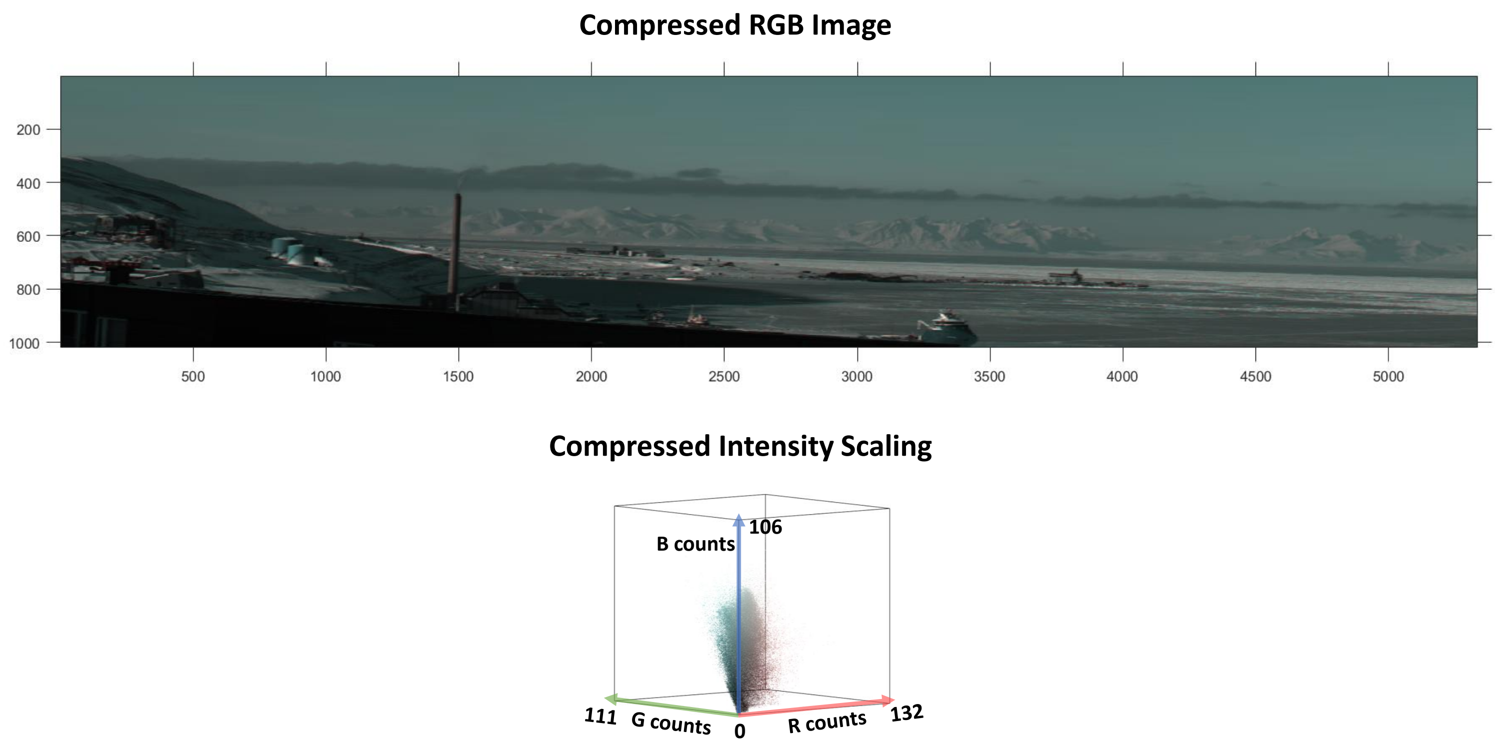

Figure 24: The image and the intensity scatter plot obtained from the x265 with a QP of 30 compressed data set.

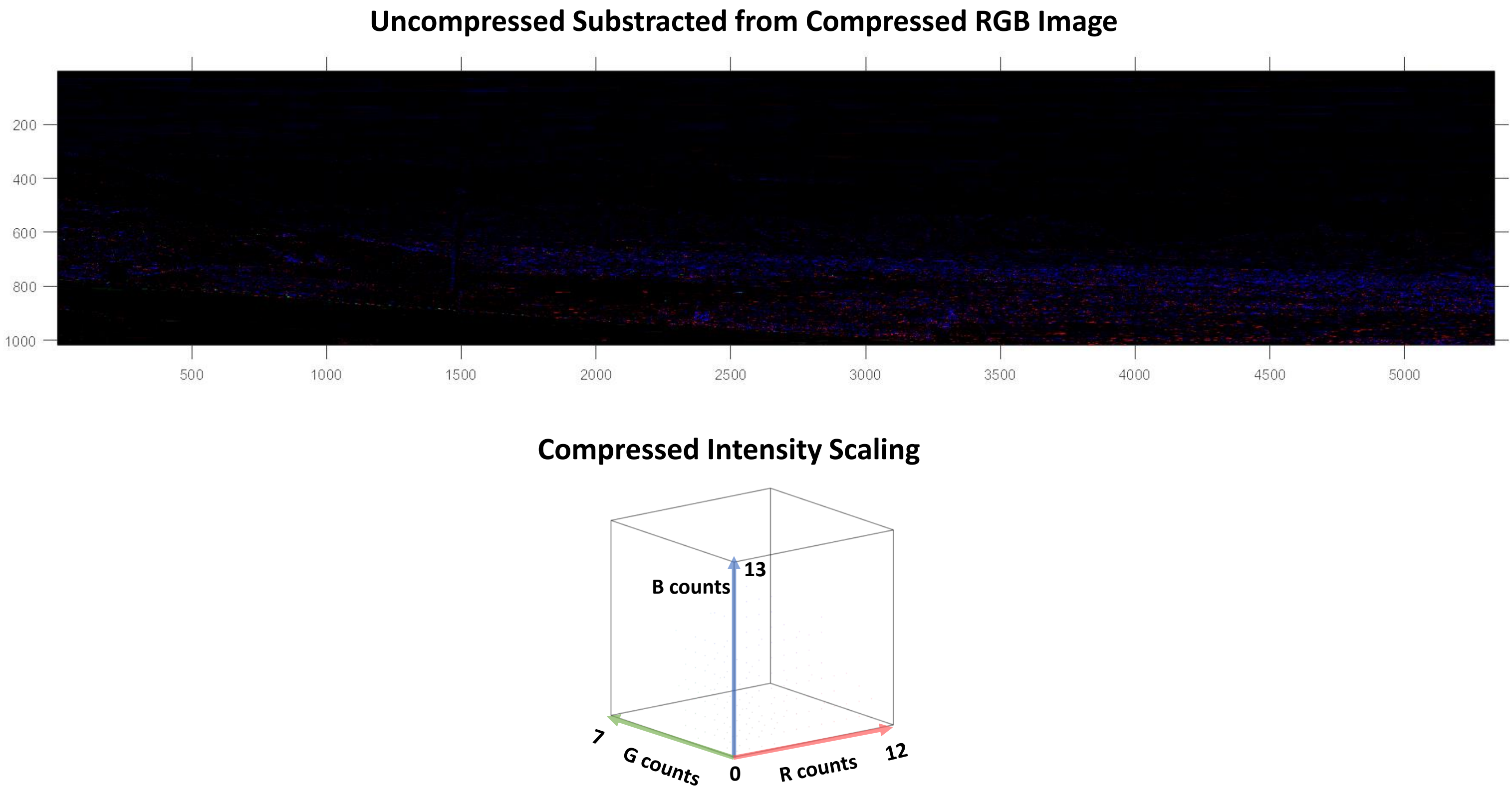

Figure 25: The difference of the uncompressed and x265 with a QP of 30 compressed data set.

Finally, an RGB-image is obtained from the measurement of the Svalbard scenery. The video from the hyperspectral imager was transformed to an hyperspectral datacube from which an RGB-image was compiled to compare visually the uncompressed reference image to an image derived from a hyperspectral data cube that was compressed with the x265 (with a QP of 30) compression algorithm. The wavelength calibration took place on frame number 601 which is a **P** frame in the compressed data file and naturally an **I** frame for the uncompressed data file. The final image acquisition is obtained by firstly performing the wavelength calibration as describe in the previous subsection. Secondly, a radiometric calibration is performed, after which a second order diffraction filter is applied. These steps are conducted the exact same way as was described by van Hazendonk [8]. Finally, an RGB-image is conducted with a bandpass of 3.5 nm and a center wavelength of blue for 527 nm, for green 550 nm and red 620 nm.

The result for the uncompressed RGB image can be seen in figure 23, along with the intensity scaling. The intensity scaling shows that in this picture the maximum amount of red counts is found to be 131. Therefore, a pixel with a maximum amount of red counts, 131, is assigned an intensity of 255. For green 119 counts in one pixel are equivalent to a green intensity of 255 and for blue 103 counts in one pixel are equivalent to an intensity of 255. The color scaling linear. In figure 24, the result for the image acquisition from the compressed data file can be seen. The intensity scaling is similar to the scaling of the uncompressed data file. By eye it is difficult to notice the difference between the compressed and uncompressed image. Therefore, the compressed data set is subtracted from the uncompressed data set. This image can be seen in figure 25, where the intensity is again scaled to the remaining amount of counts. The main differences visible are seen in the blue part of the spectrum because the picture contains more blue. With closer inspection it can be seen that the number of deviations matches the RGB channels. The little difference in intensity between the uncompressed and compressed data file is due to the neat compression of the data file.

With the same method described for the x265 compression with a QP of 30 in this section, also images are obtained for the an x265 compression with a QP of 20 (see Appendix B) and an x264 compression with a QP of 30 (see Appendix C. The compression factor of the x265 with a QP of 20 ($1.1{\cdot}10^3$), is a factor 3 smaller than the x265 QP 30 compression and shows similar results to the x265 with a QP of 30 compression.

The x264 compression with a QP of 30 (compression factor of $2.2{\cdot}10^3$) shows in the image of the difference of the compressed and uncompressed a major difference compared to the 25. This was expected from earlier results in the Hydrogen Gas Discharge and Fluorescent Tube experiments, where shifts in intensity were observed.

In Appendix D, the xvid compressed (compression factor of $4.1{\cdot}10^2$) centerline of frame number 501 can be seen. From this compression it is not possible to determine the Fraunhofer peak locations, making a wavelength calibration unreliable.

5 Conclusion

In this report experiments are conducted where the HSI V6 acquired uncompressed data. After the measurements were conducted, the data files were compressed with x264 with a QP of 30 and 20, xvid and x265 with a QP of 30. For each frame in each compressed data file it is determined if it is an **I**, **P** or **B** frame. The compression took place with *ffmpeg* [18]

For the experiments performed with a Fluorescent Tube, all compressed data files are compared to the uncompressed data file. It can be seen by eye in figures 11, 12 and 13 that the x265 compressed data file is most similar to the uncompressed data file, whereas it achieves a high compression factor, see table 1. Furthermore, it is observed that an **I**-frame conserves most detail after compression, as expected.

In the experiments performed with a Hydrogen gas discharge, the spectral position, intensity and bandpass of the H_α-peak is determined for both uncompressed and compressed data files. It can be concluded that comparing these values is an insightful method to quantitatively evaluate the performance of a compression algorithm. From these results, see figures 16, 15 and 17, it was shown that the x265 (QP30) compression is most similar to the uncompressed data file. The difference between the different frame types within a compression algorithm is not visible. One explanation is that one of the reasons for the quality loss in **P** and **B** frames, is due to moving elements in between frames, however, this was a static and stable measurement. Therefore, this measurement might not have been optimal to test for differences in compression that could occur between the different frame types.

Lastly, a wavelength calibration followed by an image acquisition from a measurement of a Svalbard scenery is performed. To perform a correct wavelength calibration, it is important to accurately detect the Fraunhofer minimums in the spectrum. The method used in this report to determine the minimum, by taking the mean of the minimums in a selected region of interest, can be improved, as can be seen in figure 19. However, even with this improvable method of minimum detection, the minimum detected in the compressed data file deviates from the detected minimum in the uncompressed data file with a maximum of only 2 pixels. After wavelength calibration, the difference in the minimum locations is less than 1 nm. The accuracy of the wavelength calibration is not improved by using a QP of 20 with this minimum detection method. This holds for all frame types. One possible explanation could be that the current minimum detection method is not optimal. Using the x265 compression algorithm with a QP of 30 for new image acquisition will therefore minimize the influence of compression on a wavelength shift. The highest compression factor is possible with a QP of 30.
With this wavelength calibration and earlier derived methods from van Hazendonk [8] and Henkriksen [9], final images are obtained for the compressed and uncompressed data files. The final images are subtracted from each other, and with a new intensity scale an image of the difference is obtained in figure 25. The differences are highly intensified and still barely visible, confirming that the x265 compression with a QP of 30 is an excellent candidate for compressing data obtained by the HSI V6, with minimum information loss.

The settings of the x265 can be varied for the purpose of experimenting. These settings depend on the application, for example how fast data has to be transmitted, what is the infrastructure of the experiment, how much energy or bandwidth is available. Depending on this, the best choice is either the x265 with a QP of 30 or x265 with a QP of 20 or even higher or lower QP settings.

6 Future Research

From this report it can be seen that the intensity is highly influenced by the compression with x264. Therefore, it is recommended to re-perform experiments with a Tungsten lamp, however, now by obtaining the data in uncompressed mode. These new results can be used for the radiometric calibration, where the radiometric calibration constant can be determined again without influence of the compression.

Another interesting result from the experiments performed with the x264 compression is that the average FWHM of the x264 compressed data set appears sharper than in uncompressed data set, implying to achieve a higher accuracy than the uncompressed data set, which is theoretically not possible. However, it is interesting to investigate in future research if this effect is due to shortcomings of the compression algorithm or because the compression algorithm filters noisy data points, resulting in a smaller bandpass. To investigate this, it would be interesting to learn more about the SNR present in images obtained with the HSI V6.

One possibility to quantitatively evaluate the effects of compression of the CCSDS-123v1 lossless compression algorithm, which is earlier investigated by [11], is by determining the index, bandpass and intensity of certain gas discharge peaks, like in figure 17.

References

[1] Dimitris G Manolakis, Ronald B Lockwood, and Thomas W Cooley. *Hyperspectral imaging remote sensing: physics, sensors, and algorithms.* Cambridge University Press, 2016. 5

[2] Geir Johnsen, Martin Ludvigsen, Asgeir Sørensen, and Lars Martin Sandvik Aas. The use of underwater hyperspectral imaging deployed on remotely operated vehicles-methods and applications. *IFAC-PapersOnLine*, 49(23):476–481, 2016. 5

[3] Astrid D Chacon, Miguel Velez-Reyes, Stephen M Escarzaga, Sergio A Vargas Zesati, and Craig E Tweedie. Analysis of close-range hyperspectral images of vegetation communities in a high arctic tundra ecosystem. In *Algorithms, Technologies, and Applications for Multispectral and Hyperspectral Imagery XXV*, volume 10986, page 109861Q. International Society for Optics and Photonics, 2019. 5

[4] Heidi Dierssen, Astrid Bracher, Vittorio Brando, Hubert Loisel, and Kevin Ruddick. Hyperspectral detection of algal diversity. *Oceanography*, 33(1):74, 2020. 5

[5] T Platt, N Hoepffner, V Stuart, and C Brown. Ioccg report number 7: Why ocean colour? *The Societal Benefits of Ocean-Colour Technology*, 2008. 5

[6] Hypso (hyper-spectral smallsat for ocean observation), 2018, https://www.ntnu.edu/ie/smallsat/mission-hyper-spectral-camera. Last accessed 8 May 2020. 5

[7] Fred Sigernes. Pushbroom hyper spectral imager version 6 (hsi v6) part list - final prototype. 2018. 5, 8, 13, 35

[8] Lotte van Hazendonk. Calibration of a hyper spectral imager. *Master Internship Report*, 2019. 5, 8, 11, 13, 25, 31, 32

[9] Marie Bøe Henriksen. Hyperspectral imager calibration and image correction. *Master Thesis*, 2019. 5, 11, 13, 25, 32

[10] Lucana Santos, Sebastián López, Gustavo M Callico, Jose F Lopez, and Roberto Sarmiento. Performance evaluation of the h. 264/avc video coding standard for lossy hyperspectral image compression. *IEEE Journal of Selected Topics in Applied Earth Observations and Remote Sensing*, 5(2):451–461, 2011. 5, 11, 15

[11] Milica Orlandić, Johan Fjeldtvedt, and Tor Arne Johansen. A parallel fpga implementation of the ccsds-123 compression algorithm. *Remote Sensing*, 11(6):673, 2019. 6, 33

[12] Giorgio Antonino Licciardi. Hyperspectral compression. In *Data Handling in Science and Technology*, volume 32, pages 55–67. Elsevier, 2020. 8, 11

[13] JM Beckers. The profiles of fraunhofer lines in the presence of zeeman splitting. *Solar Physics*, 9(2):372–386, 1969. 8

[14] Fred Sigernes. Hyper spectral imaging. *AGF-331: Remote Sensing and Spectroscopy - lecture notes.* 9, 10

[15] Robert Sedgewick and Philippe Flajolet. *An introduction to the analysis of algorithms.* Pearson Education India, 2013. 11

[16] Khalid Sayood. *Introduction to data compression.* Newnes, 2012. 11, 12, 15

[17] Thomas Wiegand, Gary J Sullivan, Gisle Bjontegaard, and Ajay Luthra. Overview of the h. 264/avc video coding standard. *IEEE Transactions on circuits and systems for video technology*, 13(7):560–576, 2003. 15

[18] FFmpeg Developers. *ffmpeg tool (Version be1d324) [Software].* Available from http://ffmpeg.org/, 2016. 16, 32

A Experimental Equipment

Item	Description
1	50 mm VIS-NIR lens (Front, Collimator and Detector lenses)
2	25mm Sq. 17.5deg. Blazed Trans. grating (300 lines/mm) 1
3	Adapter ring SM1 C-mount internal
4	SM1 lens tube 1 inch long with internal threads.
5	30 mm Cage plate - SM1 tubes
6	Fixed high precision mounted slit
7	C-mount 30 mm cage plate (NTNU sensor board)
8	30 mm Cage plate 35 mm aperture (iDS-mount)
9	4 x Steel rods 1.5 inch long
10	4 x Steel rods 1.0 inch long
11	4 x Rod End Swivels
12	DMK 33UX174 camera head
13	C-mount 0.25 2 mm space ring kit (2 each)

Table 3: Part list of the HSI V6, obtained from [7].

B Wavelength Calibration x265 QP of 20

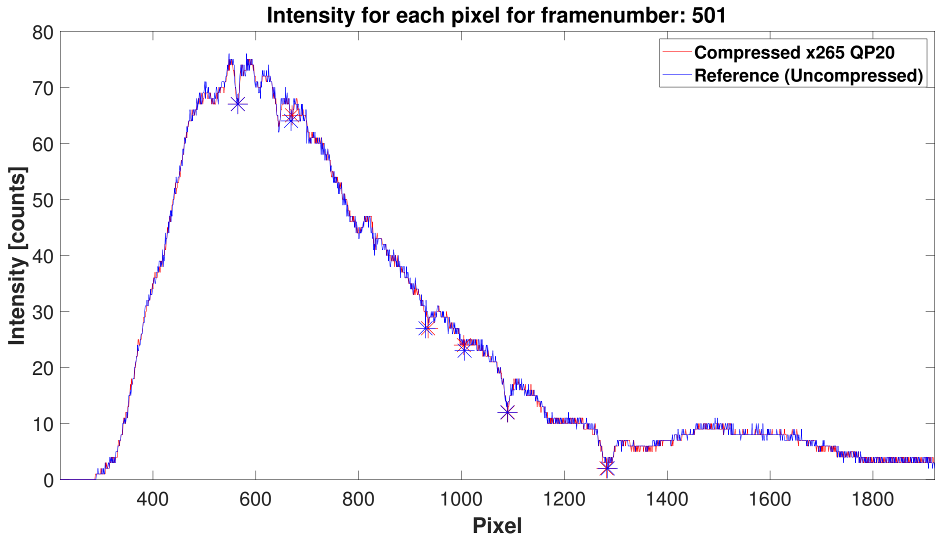

Figure 26: The x265 with a QP of 20 compressed and uncompressed centerline of frame number 501 (**I**-frame), from a measurement of a view of the port of Svalbard, can be seen here. It can be seen that the centerlines nicely overlap.

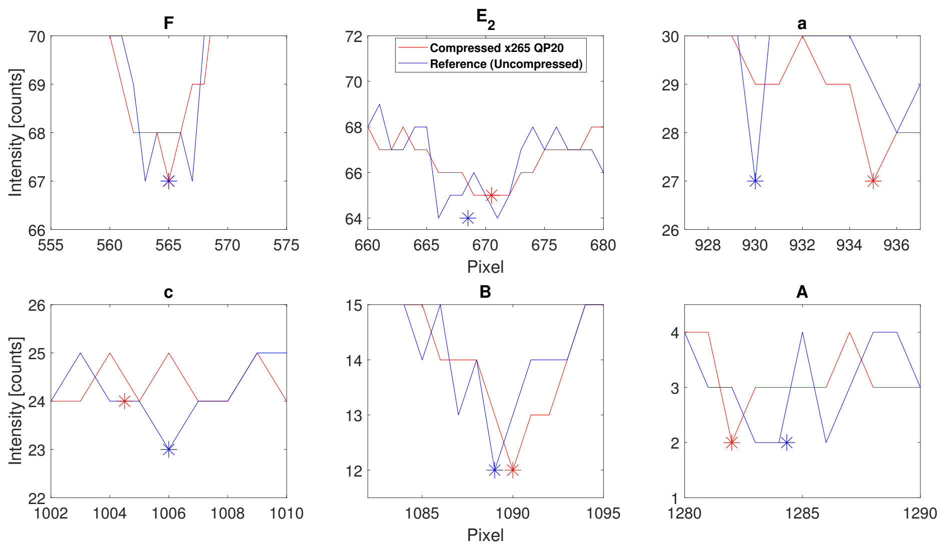

Figure 27: Within a certain pixel range it is recognized that a Fraunhofer line is present, for example the Fraunhofer line F is recognized to be in the pixel range of 555 and 575. This detected minimum (star) can be seen on the top left of the images, followed by the E_2, a, c, B and A location. It can be seen that the detected minimums of the compressed and uncompressed data sets are not equivalent.

B.1 Obtained Images x265 QP of 20

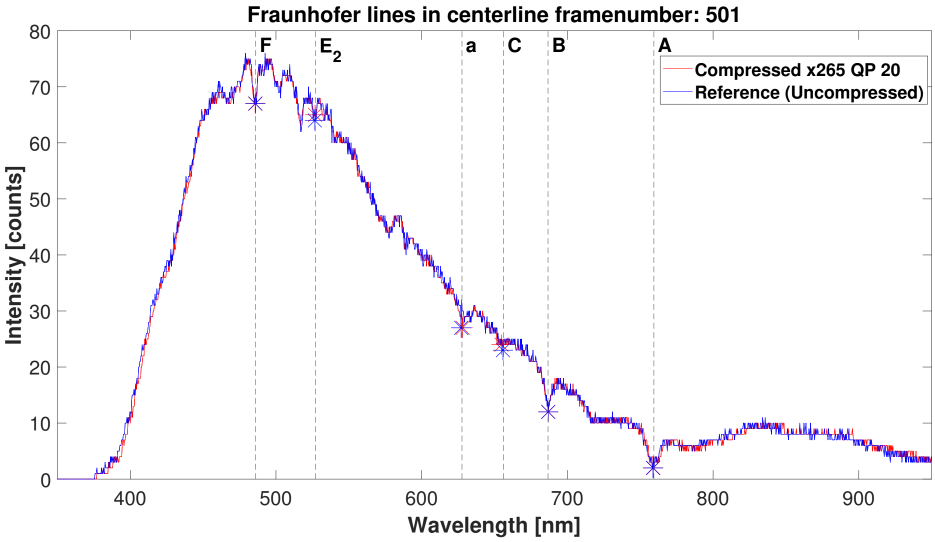

Figure 28: The x265 with a QP of 20 compressed and uncompressed centerline of frame number 501 (**I**-frame), from a measurement of a view of the port of Svalbard, after wavelength calibration can be seen here. It can be seen that the centerlines nicely overlap. The Fraunhofer lines F, E_2, a, c, B and A on which the wavelength calibration took place, are also shown in dotted vertical lines.

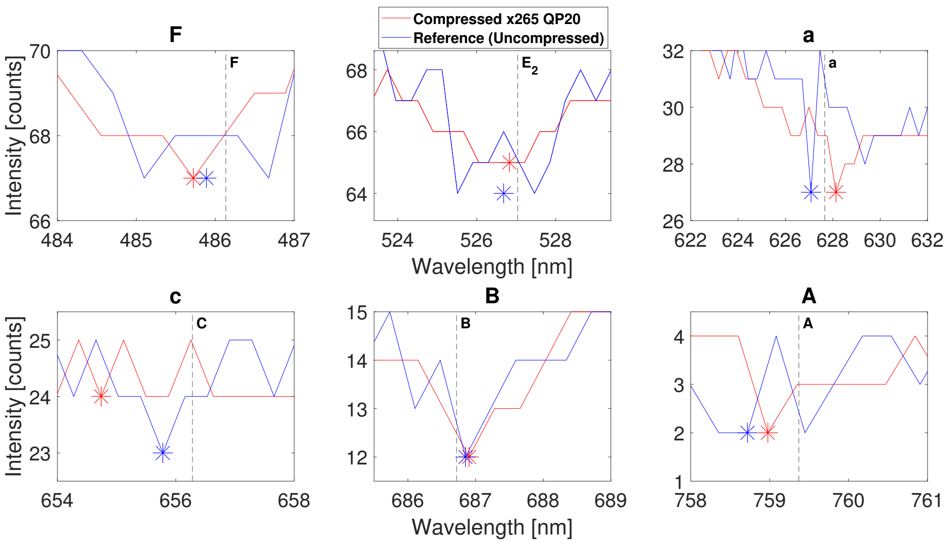

Figure 29: The detected minimums (star), that are used to perform the wavelength calibration are shown here. The Fraunhofer lines used are F, E_2, a, c, B and A and are marked with a vertical dotted line. It can be seen that the detected minimums of the compressed and uncompressed data set are not equivalent.

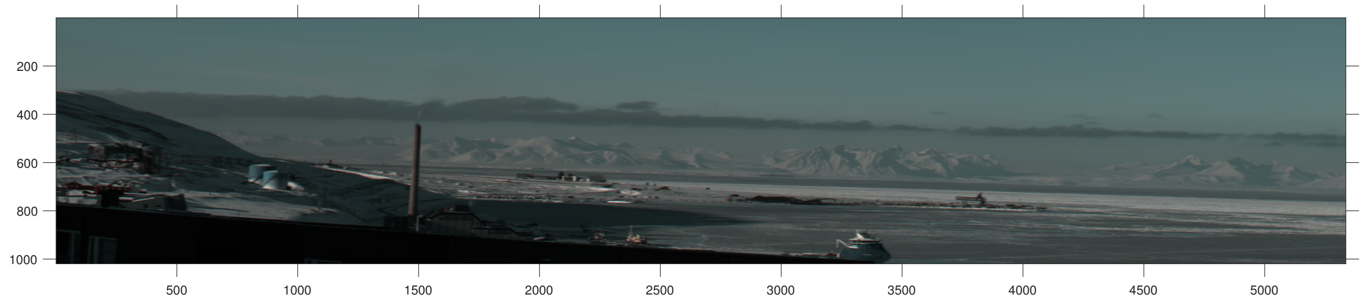

Figure 30: Image obtained from a x264 compressed data set with a QP of 20.

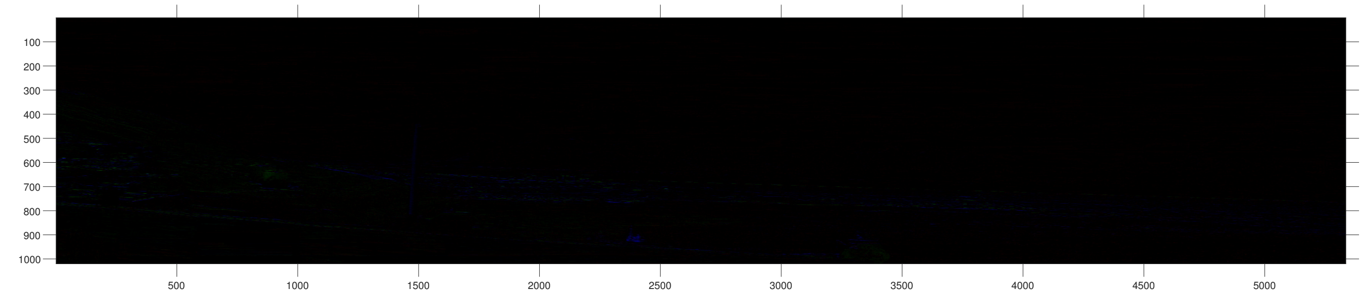

Figure 31: The difference of the uncompressed and x265 with a QP of 20 compressed data set, showing a very similar result as with the x265 with a QP of 30 compression, see figure 33

C Obtained Images x264 with a QP of 30

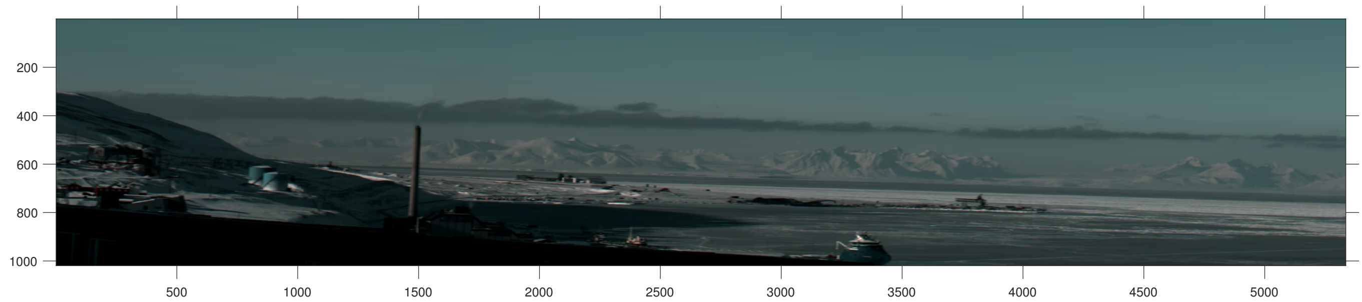

Figure 32: Image obtained from a x264 compressed data set with a QP of 30.

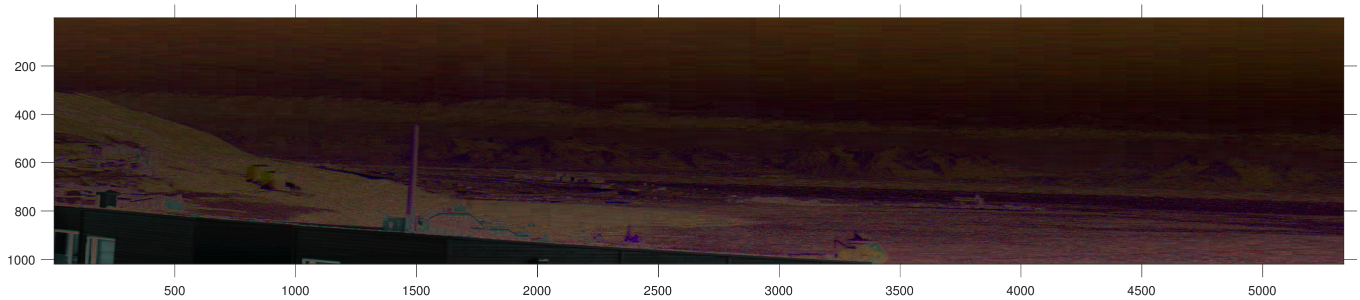

Figure 33: The difference of the uncompressed and x264 with a QP of 30 compressed data set. A more clear picture can be observed compared to the compression with x265 with a QP of 30 (figure 25), showing that more information is lost compared to the x265 compression.

D Peak Determination xvid/x263

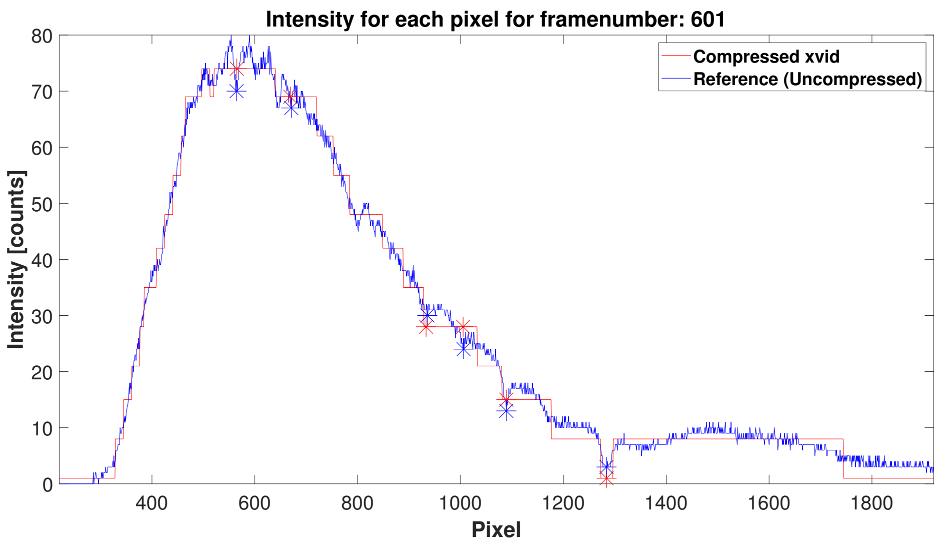

Figure 34: The xvid compressed and uncompressed centerline of frame number 501 (**I**-frame), from a measurement of a view of the port of Svalbard, can be seen here. It can be seen that the intensities of the centerlines nicely overlap, however, too much detail is lost for a reliable detection of Fraunhofer peaks.

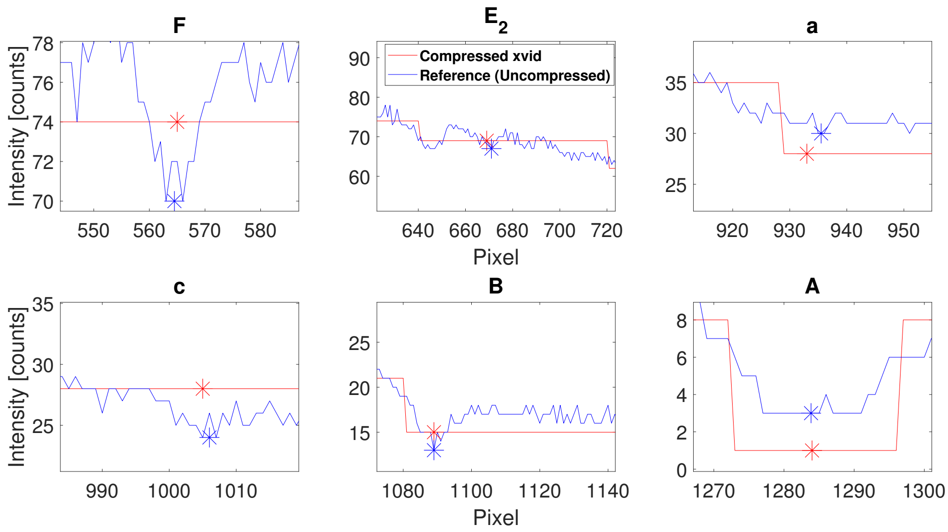

Figure 35: Without having the uncompressed data set, it would be impossible to determine the Fraunhofer peaks in the xvid compressed data set.